Applied Environmental Research
- RESEARCH FOR SUSTAINABLE PLANET -

Research Article

Landslide Susceptibility Mapping via Dempster-Shafer, Statistical Index, and Certainty Factor Models in GIS and Their Comparison at Pidie Recency in Aceh, Indonesia

Septianto Aldiansyah*, Amniar Ati, Fitriyani Saudi

Department of Geography Education, Faculty of Teacher Training and Education, Universitas Halu Oleo, Indonesia

*Corresponding Email: septianto.aldiansyah@uho.ac.id

Abstract

Landslides are natural disasters that are active if there is an interaction of environmental factors that are considered to control them, especially in mountainous areas. This study developed a landslide susceptibility map in Pidie Regency via the Dempster-Shafer (DS), statistical index (SI), and certainty factor (CF) models. A total of 957 landslide events were mapped, 70% of which were used for modeling, whereas the remaining events were used to validate the model output. Fourteen layers of conditioning factors were used: elevation, slope, aspect, curvature, TWI, SPI, STI, NDVI, rainfall, distance from river, distance from road, distance from fault, LULC, and lithology. To assess model performance, the model output was then compared with validation landslide data that had been separated from previous training data. Therefore, the receiver operating characteristic (ROC) curve was used, and the area under the curve (AUC) was calculated via the success rate and prediction rate curves. The results show that the CF model has the best performance, with success rates and prediction rates of 81.02% and 80.55%, respectively, followed by DS (80.25% and 78.70%) and SI (76.58% and 75.93%). Therefore, the CF model is more accurate than the DS and SI models. The resulting landslide susceptibility map can be used for early land use planning and hazard mitigation purposes.

ARTICLE HISTORY

Received: 13 Jun. 2025
Accepted: 19 Sep. 2025
Published: 15 Oct. 2025

KEYWORDS

Landslide;
Susceptibility map;
Dempster–Shafer;
Statistical index;
Certainty factor;
Pidie

Introduction

One type of natural disaster that has a destructive effect is land movement or landslides [1]. Natural and anthropogenic factors influence this movement, and these factors are considered important for assessing, predicting, and delineating landslide potential [2]. Landslides are considered to damage facilities and infrastructure, such as engineering structures, buildings, vital resources, electricity networks, important land covers (e.g., forests and grasslands), agricultural areas, and mines, and ultimately cause sediment and mudflows and shallow dams. This effect continues to have social impacts where immigration and unemployment are aspects that cannot be ignored [3]. Landslides are quite common in Indonesia. Mountainous areas are quite dominant in Indonesia, and landslides are considered to be natural disasters that cause many fatalities and property damage [4]. This phenomenon has been widely studied in Indonesia, and the costs used for mitigation and early warning systems are not comparable to the losses incurred [5]. Given the crucial impact of landslides on resources, residential areas, and large amounts of soil erosion, it is necessary to detect and zone potential landslides and predict landslides to minimize geological hazards and develop mitigation methods [6]. Geographic information systems play an important role in this regard, considering that GIS is the main interpretation tool that is quite efficient and effective in determining vulnerability zones with its statistical models [7]. Landslide mapping is the main objective of this process [8]. The use of data-based models requires three main principles in zoning and predicting landslide vulnerability

https://doi.org/10.35762/AER.2025034

correctly. These three principles are governed by the following assumptions [9–10]: (1) landslide inventory maps (based on the fact that past and present events are the main keys in generalizing and predicting the future) [9–11], (2) Selection of conditioning factors appropriately (these data must be based on the truth as factors that influence landslide events and are independent without overlapping information) and (3) Appropriate models for zoning landslide susceptibility [9–10,12] are used.

Although much progress has been made in mapping landslide hazards, several limitations remain [13]. A number of data-driven approaches have been proposed to map landslide susceptibility and hazard zoning. These approaches are grouped into definitive (deterministic) and probabilistic (nondeterministic) categories [14]. Nondeterministic methods are based on various heuristics, bivariate [15] and multivariate [16] statistical and probabilistic analyses [16–17], and expert knowledge [18]. The certainty factor (CF) [19] and statistical index (SI) [20] are examples of bivariate methods, whereas Dempster–Shafer (DS) (governed by the theory of Bayesian) [21–24] is considered a probabilistic method.

Currently, the capabilities of various bivariate [25–26], multivariate [25, 27–28], probabilistic [29–30], knowledge-based [31], IoE [25, 32] and DS methods [33–34] are continuously evaluated and compared. The DS, SI, and CF theories are equally important for quantifying information system uncertainty. DS theory was initially developed by Dempster using the concept of probabilistic upper and lower bounds, which is then known as a hypothesis. Uncertainty creates a clear difference in the assessment and comparison among the DS, SI, and CF theories. The DS model is quite advantageous when analyzing uncertainty in relation to conventional theory [34]. In addition, the uncertainty and the representation and combination of various evidence obtained from various sources are other advantages of this method. On the other hand, the SI method is a widely applied statistical approach for landslide modeling that relies on the ratio of landslide occurrence to different classes of conditioning factors. While the SI does not explicitly quantify uncertainty in a probabilistic sense, it captures the strength of the association between landslide presence and specific factor classes through frequency analysis. This method is simple, data-driven, and reproducible, making it suitable for data-rich environments [35,36]. However, SI is often limited in dealing with conflicting or uncertain evidence, as it lacks mechanisms for handling inconsistency between input sources. CF provides a heuristic-based approach to address uncertainty in expert judgment, enabling the combination of multiple evidential layers with positive or negative contributions. The main reason for the usage of CF is its flexibility in representing subjective knowledge, particularly in situations where probabilistic information is incomplete or lacking [37]. Additionally, CF allows for the integration of expert-derived or empirical data with controlled uncertainty propagation. On the basis of the advantages of each model, a comparison of the three still needs to be performed. The assessment and comparison of these models can provide more beneficial and valid results for zoning landslide susceptibility in natural systems.

The Pidie Regency is located in Aceh Province and has highly specific and complex active environmental and geological characteristics [38]. This condition makes this area vulnerable to landslides. Landslide vulnerability analysis methods have been widely studied in Aceh, most of which are concentrated in the central and northern parts of the region. In addition, research conducted in Pidie Regency has also been assessed at the local scale. Although local-scale research remains important as a micro basis for validation, it must also be part of a broader study framework. Land-use change and urbanization are significant effects that can exacerbate landslide vulnerability, particularly in areas with rapid population growth and development. Previous studies have shown that urban expansion and land-use change significantly impact slope stability and hazard intensity [39–41].

Research comparing prediction accuracy, especially the differences in model performance under different modeling datasets, is lacking in this area. Studies on the impacts of economic consumption, energy conservation, and environmental protection on disaster prevention and control are even rarer. In this study, a single prediction model was constructed by combining statistical analysis and GIS technology. By comparing the prediction results, accuracy, and performance of various models, we explore ways to evaluate geological hazard vulnerability and reduce disaster management costs. This aims to avoid unnecessary waste of human, material, and financial resources in disaster prevention and control and achieve long-term sustainable development.

Therefore, Pidie Regency was chosen for the analysis and comparison of statistical models of various environmental and geological characteristics of the region in connection with its area, which is on an active fault line and close to a subduction zone. The lack of landslide zoning in this area and comparisons among DS, SI, and CF have also not been studied thoroughly. Thus, the main objective of this study is to develop, assess, and validate landslide susceptibility maps in Pidie Regency through DS, SI, and CF models, where the models are built via landslide conditioning factors. Relative importance is also examined in this study. This study also compares the performance of these models, evaluates their implications for mitigation strategies, and positions the results within the sustainability and resilience agenda.

Materials and methods

1) Study area

The research area is located in Pidie Regency, Aceh Province, Indonesia, with an area of 318,349.11 ha. Geographically, this area is located between 4°30' and 4°60' North Latitude and 95°75' and 96°20' East Longitude (Figure 1). The research location is at an altitude of 0–2788 masl. Most of the area is covered by primary forest, with population centers spread across the Pidie, Mutiara Timur, Padang Tiji, Indrajaya, and Simpang Tiga districts. The climate regime and terrain complexity are more heterogeneous. The geology of Pidie Regency generally consists of young alluvium deposits originating from river and coastal deposits. These deposits consist of various types of sediments, such as gravel, sand, claystone, and mud. In addition, the Kotabakti Formation, which includes mudstone, calcareous siltstone, sandstone, conglomerate, and tuff, is present in Pidie Regency. The annual rainfall reaches 1,532 mm per year, with July and November having the lowest and highest precipitation values of 140 mm and 325 mm, respectively, and the average temperature ranges from 24°C–32°C [42].

2) Data collection and interpretation

The data used in this study are sourced from organizations and field investigation results. Lithology maps were obtained from the geological map of the Indonesian Ministry of Energy and Mineral Resources. SRTM-DEM data with a spatial resolution of 30 m were used to extract elevation, slope, aspect, curvature, topographic wetness index (TWI), stream power index (SPI), and sediment transport index (STI) information. Rainfall data were obtained from WorldClim version 2.1. The normalized difference vegetation index (NDVI) map was obtained from Landsat 8 imagery with a resolution of 30 meters. The land use/land cover map was obtained from the Ministry of Environment and Forestry in 2023. The road, river, and fault factor maps were obtained from the Geospatial Information Agency at a scale of 1:25,000. All the data were built with ArcGIS 10.4.1, where the entire process was carried out in the ArcGIS environment. The DS, SI, and CF models were used to generate landslide susceptibility maps. Landslide susceptibility assessment and validation were carried out via the AUC method (Figure 2).

3) Landslide inventory map

Landslide inventory maps, including technical reports, government reports, and expert interviews, were obtained through field surveys, aerial photography, Google Earth, satellite imagery, and article searches [43]. This study used 957 landslide areas from GPS-integrated data sources for 2018-2024. The types of landslides identified were caused by rainfall (954 locations) and earthquakes (53 locations). These data were grouped into training and validation sets (Pradhan and Buchroithner, 2010), with 70% (670 locations) used for training and 30% (287 locations) used for validation [44].

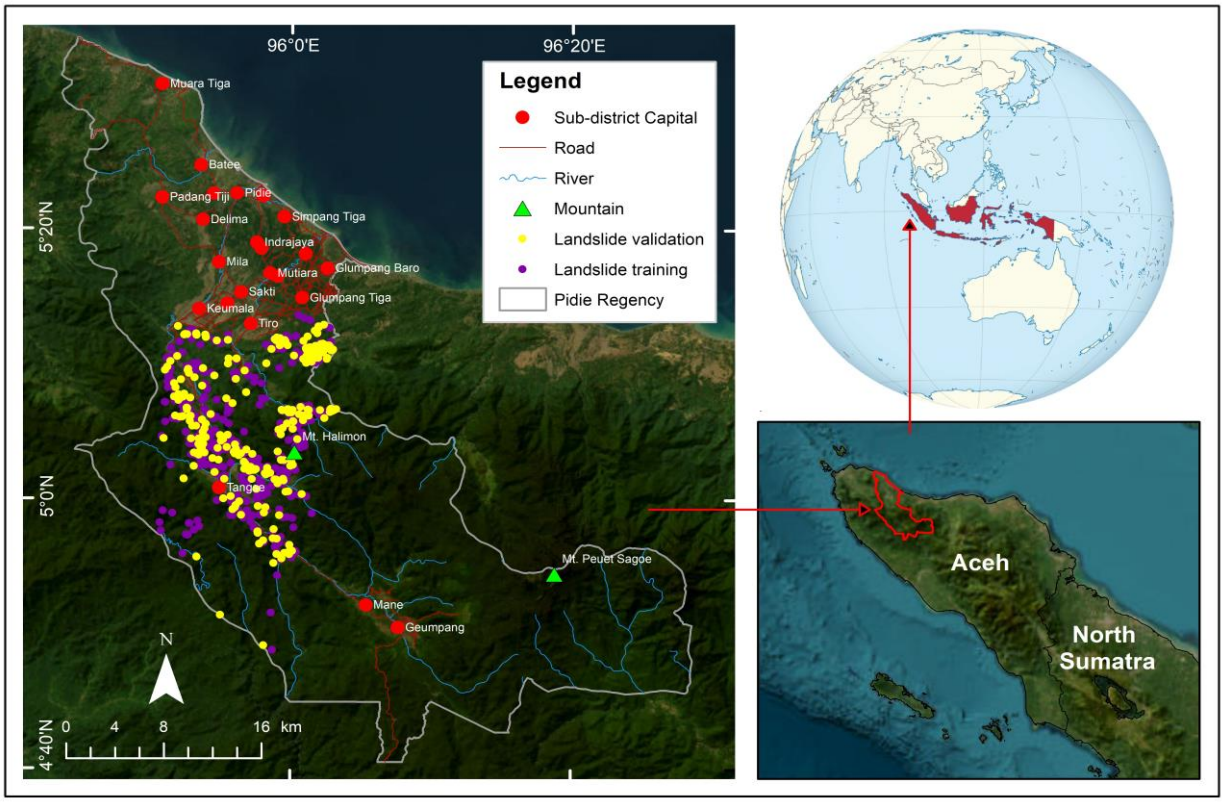

Figure 1 Map of research locations.

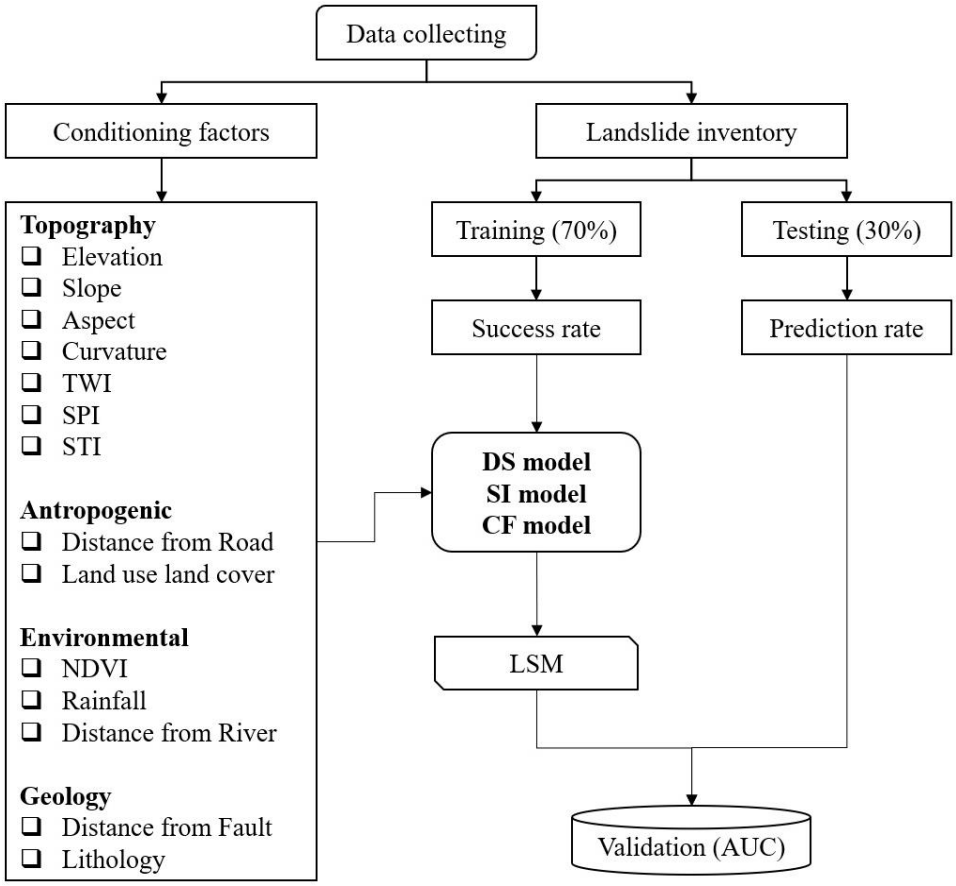

Figure 2 Flowchart of landslide susceptibility in the Pidie Regency.

4) Landslide conditioning factors

Landslide conditioning factors in each region have different triggering effects. These triggering factors are grouped into two main and secondary or subsequent groups [9, 11]. The group is then divided into four categories, namely, geomorphology, geology, hydrology, and anthropogenic [8, 27]. The initial step in zoning and assessing landslide susceptibility is the selection of appropriate conditioning factors, although this remains a major challenge because there are no standard rules governing this process [45]. In general, intrinsic slope, aspect, and lithology factors are considered consistent with landslide susceptibility, whereas other factors are still debated. However, researchers usually link geographic characteristics and analysis techniques with the type of landslide that occurs to determine this step [6, 46–47].

The number of conditioning factors used sometimes varies from a few [35, 46, 48] to several [44, 49]. A large or small number will not always produce prediction results with high accuracy [47]. In fact, the quality of the model decreases when noise factors are included [46–47]. This study used 14 landslide conditioning factors determined from the literature [8, 17, 25, 44–47, 50], as well as the geographical conditions of the study area. These factors include elevation, slope, aspect, curvature, TWI, SPI, STI, NDVI, rainfall, proximity (river, road, and fault), LULC, and lithology. Slope instability is considered to be caused by geomorphometric and geomorphological processes. Therefore, factors derived from DEM data are generated.

Elevation is considered the most frequently used parameter in landslide susceptibility mapping [51]. Landslides can occur on certain reliefs, while reliefs can be extracted from elevation and classified into ten classes at 300 m intervals (Table 1; Figure 3a). Slope is also often used in landslide assessment [52] because this factor strongly affects slope instability [53]. The shear stress increases with increasing slope gradient [54] because of its correlation with gravity. Therefore, the probability of landslide occurrence also increases with the steepness of the slope [27]. The slope is extracted from SRTM data and classified into 5 classes (Table 1; Figure 3b). Aspect is an important parameter in landslide mapping [15]. This parameter is actually related to the microclimate, such as sun exposure, wet or dry winds, and rainfall intensity, thus causing differences in soil moisture and affecting slope stability [8,15]. The aspect is also generated from SRTM data and classified into 9 classes (Table 1; Figure 3c). Curvature is a crucial parameter in landslide body studies. Curvature refers to the unification of planes on the surface [55], which is responsible for providing driving and opposing pressures on the landslide area [56]. In this study, curvature is classified into three classes (Table 1; Figure 3d).

Table 1 Classes from the 14 conditioning factors of landslides

Conditioning factors	Classes
Elevation (m)	(1) 0-100; (2) 100-400; (3) 400-700; (4) 700-1000; (5) 1000-1300; (6) 1300-1600; (7) 1600-1900; (8) 1900-2200; (9) 2200-2500; (10) 2500-2788
Slope (%)	(1) 0-8; (2) 8-15; (3) 15-25; (4) 25-45; (5) >45
Aspect	(1) Flat; (2) North; (3) Northeast; (4) East; (5) Southeast; (6) South; (7) Southwest; (8) West; (9) Northwest
Curvature	(1) Concave; (2) Flat; (3) Convex
TWI	(1) <8; (2) 8-12; (3) >12
SPI	(1) -1-3; (2) 3-7; (3) 7-11; (4) 11-14; (5) 14-17
STI	(1) <-1; (2) -1-61; (3) 61-185; (4) 185-497; (5) >497
Distance from road (m)	(1) 0-100; (2) 100-200; (3) 200-300; (4) 300-400; (5) 400-500; (6) >500
LULC	(1) Hp; (2) Hs; (3) B; (4) Pk; (5) Pm; (6) T; (7) S; (8) A; (9) Pt; (10) Pc; (11) Sw; (12) Tm; (13) Tr; (14) Pb
NDVI	(1) -2-0.1; (2) 0.1-0.3; (3) 0.3-0.5; (4) 0.5-0.7; (5) 0.7-0.9
Rainfall (mm per year)	(1) <2000; (2) 2000-2250; (3) 2250-2500; (4) 2500-2750; (5) 2750-3000; (6) 3000-3250; (7) >3250
Distance from river (m)	(1) 0-200; (2) 200-400; (3) 400-600; (4) 600-800; (5) >800
Distance from fault (m)	(1) 0-1000; (2) 1000-2000; (3) 2000-3000; (4) 3000-4000; (5) 4000-5000; (6) 5000-6000; (7) 6000-7000; (8) >7000
Lithology	(1) Qh; (2) Tb; (3) Mumb; (4) Tbg; (5) Qtpsl; (6) Mullr; (7) Tuktm; (8) Bps; (9) Tukts; (10) Tsn; (11) Tlmj; (12) Misk; (13) Miski; (14) Qvo; (15) Tps-me; (16) Tps-sa; (17) Ttb; (18) Tla; (19) Tmg; (20) Tbs; (21) Mutlr; (22) Mugl; (23) Tgm; (24) Tjl; (25) Tukt; (26) Tk; (27) Mum; (28) Tlm; (29) Qtps; (30) Tsm; (31) Tsp; (32) Tib; (33) Tbi; (34) Ppm; (35) Tmigs; (36) Mirb; (37) Tl; (38) Qm; (39) Mpn; (40) Tuset; (41) Kus

Note I: Qh=Young alluvium; Tb=Limestone Member; Mumb=Bengga Limestone Member; Tbg=Geumpo Limestone Member; Qtpsl=Lam Kabue Limestone Member; Mullr=Reef Limestone Member; Tuktm=Meuh Member; Bps=Padang Tiji Member; Tukts=Pintu Satu Member; Tsn=Senong Member; Tlmj=Meujeumpo Member; Misk=Sikuleh Batholith; Miski=Sikuleh Batholith (old complex); Qvo=Olim Volcanic Rocks; Tps-me=Peuet Sague Volcanic Rocks, Me unit; Tps-sa=Peuet Sague Volcanic Rocks, Sa unit; Ttb=Temba Volcanic Rocks; Tla=Agam Formation; Tmg=Meugeur Volcanic Rock Formation; Tbs=Sitoptop Limestone Formation; Mutlr=Teunom Limestone Formation; Mugl=Geumpang Formation; Tgm=Gume Formation; Tjl=Jeleum Formation;
Note II: Hp=Primary dryland forest; Hs=Secondary dryland forest; B=Scrub; Pk=Plantation; Pm=Settlement; T=Bare land; S=Savanna; A=Water body; Pt=Dryland agriculture; Pc=Mixed dryland agriculture; Sw=Rice field; Tm=Aquaculture pond; Tr=Transmigration area; Pb=Mining area

The TWI and SPI are indices that describe the combined effects of topography and hydrology. Both contribute to the effects of erosion or soil conservation [57]. The SPI is usually expressed in terms of the erosive power of water flow, where the discharge is assumed to be proportional to the catchment area [57]. The SPI is calculated via Eq.1 as follows:

$$\mathrm{SPI} = \mathrm{As} \times \tan\sigma \qquad \text{(Eq.1)}$$

where σ is the slope angle (in degrees). The SPI is the gravitational force on sediments where movement is consistent with the movement of solid grains. This condition is considered to increase the instability of the slope direction [29,58]. The SPI is reclassified into five classes via Eq.1 (Table 1; Figure 4f).

The TWI indicates the influence of topography on the size and location of saturated source areas of runoff initiation [57]:

$$\mathrm{TWI} = \ln\left(\frac{\mathrm{a}}{\tan\sigma}\right) \qquad \text{(Eq.2)}$$

where a is the cumulative upslope area that drains to a point (per unit contour length) and where σ is the slope angle (in degrees). The TWI describes the function of the slope and flow direction (Figure 3e). Therefore, this factor is considered significant in influencing slope instability [29, 58]. The TWI is reclassified to obtain three classes through Eq. 2 (Table 1; Figure 3e). The STI measures the erosion and transportation capacity of a river [29] (Figure 3g). Strong water flow and steep slopes carry more sediment and easily erode soil, which ultimately affects slope instability. STI is classified into five classes (Table 1; Figure 3g). The STI is calculated via Eq. 3 as follows:

$$\mathrm{STI} = \left[\frac{\mathrm{A}}{22.13}\right]\left[\frac{\sin(\beta)}{0.0896}\right]^{1.3} \qquad \text{(Eq.3)}$$

where A is the upstream catchment area and where β is the slope steepness in degrees.

Distance from roads is one of the most important anthropogenic factors affecting landslide occurrence [19,23]. The closer to the road, the greater the potential for landslides because human activities and morphological

changes are considered to trigger slope instability. The distance from the road was classified into six classes with 100 m intervals (Table 1; Figure 3h). Human land use changes also greatly affect slope stability [8, 15] Therefore, this parameter is always applied in landslide susceptibility assessment. This study uses fourteen classes (Table 1; Figure 3i).

The NDVI is widely used when assessing landslide susceptibility processes [25]. The NDVI describes the condition of vegetation cover. These data are extracted via the extraction technique from the near infrared and red bands of Landsat 8 OLI images and classified into five classes with an interval of 0.2 (Table 1; Figure 3j). The NDVI is calculated via Eq.4 as follows:

$$\mathrm{NDVI} = \frac{\mathrm{NIR}-\mathrm{R}}{\mathrm{NIR}+\mathrm{R}} \qquad \text{(Eq.4)}$$

where NIR and R are the spectral responses in the near infrared and red bands, respectively.

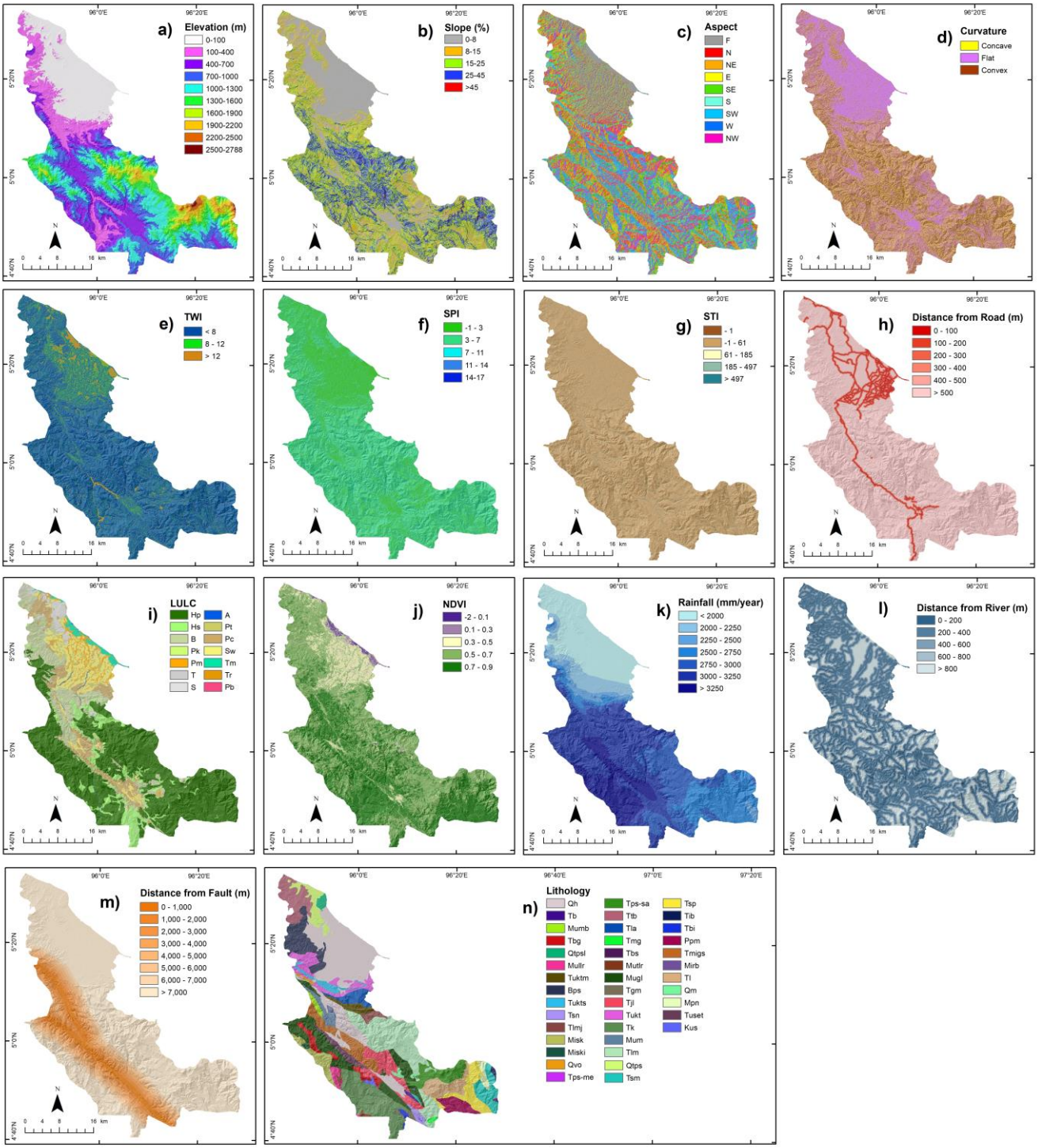

Figure 3 Conditions for landslide susceptibility analysis: a) elevation, b) slope, c) aspect, d) curvature, e) TWI, f) SPI, g) STI, h) distance from road, i) LULC, j) NDVI, k) rainfall, l) distance from river, m) distance from fault, and n) lithology

Rainfall is considered to trigger landslide susceptibility because it can increase the underground hydrostatic level and water pressure [56]. Rainfall is classified into seven classes with intervals of 250 mm (Table 1; Figure 3k). Distance from rivers has a significant effect on slope instability in mountainous areas because of water flow and overflow [15, 19, 24–25]. In this study, the distance from the river was generated via the Euclidean distance method and classified into five classes with 200 m intervals (Table 1; Figure 3l).

Faults are responsible for reducing rock strength due to tectonic faults, which trigger most landslides [19]. The distance from the fault was classified into eight classes with 1000 m intervals (Table 1; Figure 3m). Lithology is the most common conditioning factor for landslide susceptibility mapping, and each lithological unit has different influences according to geotechnical characteristics, mechanical specifications, and erosion actions [18–19]. The study area is a combination of active tectonic locations, long geological history, volcanic activity, processes, sedimentation, and complex geological structures (Table 1; Figure 3n).

5) Landslide vulnerability model

5.1) Dempster-Shafer model

The Dempster–Shafer (DS) model was developed from Bayesian probabilistic theory [33]. This model combines the belief of predetermined conditioning factors and their relative flexibility in considering uncertainty [33, 60]. Discerment is traced through DS theory to identify landslide susceptibility [23] with Eq.5.

$$m = 2^{\Theta} = [\phi, T_P, \overline{T}_P, \Theta] \text{ with} \Theta = [T_P, \overline{T}_P] \quad \text{(Eq.5)}$$

where T_P is the location affected by future landslides in pixel P and where $\overline{T}_P$ is the opposite proportion of locations that will not be affected by future landslides at each pixel P [21].

DS theory defines the mass function in identifying landslide susceptibility via the relationship between conditioning input factors and known landslides. Therefore, the probability ratio function and landslide susceptibility are used in calculating the mass function when distinguishing vulnerable and nonvulnerable areas. The ratio function of vulnerable and nonvulnerable areas can be emphasized in its contrast. Each selected layer is based on the spatial data layer in the area selected as evidence $B_i = (i = 1, 2, \dots, l)$ for the proposed target T_P. The likelihood ratio $\lambda(T_P)B_{ij}$ (Eq.6) to verify the intended positive target is as follows [21, 24]:

$$\lambda(T_P)B_{ij} = \frac{\frac{N(A \cap B_{ij})}{N(A)}}{\frac{N(B_{ij}) - N(A \cap B_{ij})}{N(C) - N(A)}} \quad \text{(Eq.6)}$$

where B_{ij} is the j-th attribute class of the evidence B_i, $N(A \cap B_{ij})$ is the number of landslide pixels occurring in B_{ij}, $N(B_{ij})$ is the density of pixels in B_{ij}, $N(A)$ is the total number of landslides occurring in the study area, and $N(C)$ is the number of pixels in the whole study area C. The ratio of landslide occurrences in attribute B_{ij} is the numerator, and the ratio of nonvulnerable landslides in that attribute is the denominator. Therefore, the likelihood ratio for the support proposition of the opposite target in Eq.7 is as follows:

$$\lambda(\overline{T}_P)_{B_{ij}} = \frac{\frac{N(A) - N(A \cap B_{ij})}{N(A)}}{\frac{N(C) - N(A) - N(B_{ij}) + N(A \cap B_{ij})}{N(C) - N(A)}} \quad \text{(Eq.7)}$$

The numerator and denominator are the ratios of nonsusceptible and susceptible areas to the attribute B_{ij}. All likelihood ratio values of class attributes of the evidence B_i are divided by the likelihood ratio to satisfy the standard conditions (Eq.6) and consider the relative importance of class attributes [21]:

$$m = 2^{\Theta} \longrightarrow [0, 1] \begin{cases} m(\phi) = 0 \\ \sum_{T \subset \Theta} M(T) = 1 \end{cases} \quad \text{(Eq.8)}$$

$$m\,(T_p)_{B_{ij}} = \frac{\lambda(T_P)_{B_{ij}}}{\sum \lambda(T_P)_{B_{ij}}} \ (\text{Belief function}) \quad \text{(Eq.9)}$$

$$m\,(\overline{T}_p)_{B_{ij}} = \frac{\lambda(\overline{T}_P)_{B_{ij}}}{\sum \lambda(\overline{T}_P)_{B_{ij}}} \ (\text{Disbelief function}) \quad \text{(Eq.10)}$$

$$(\text{Uncertainty function})\ m(\Theta) = 1 - m\,(T_p)_{B_{ij}} - m\,(\overline{T}_p)_{B_{ij}} \quad \text{(Eq.11)}$$

The belief function to support positive target propositions is obtained from the mass function $m\,(T_p)_{B_{ij}}$ (Eq.9). $1 - m\,(T_p)_{B_{ij}}$ can be applied to calculate the plausibility function. The constraints in identifying landslide events are used separately in determining the belief and plausibility functions on the basis of the likelihood ratio function.

This model is a combination of belief, disbelief, uncertainty, and plausibility functions, all of which range from 0 to 1 [33], considering that the theoretical basis is evidence function estimation [61]. The upper and lower limits of the probability are belief values that are equivalent to the mass function of $m\,(\overline{T}_p)_{B_{ij}}$ and plausibility [22, 33]. The uncertainty function $m\,(\theta)_{B_{ij}}$

(Eq.11) is an equation that expresses the difference between belief and plausibility. The disbelief function (Eq.10) is the belief in the lack of correctness on the basis of existing evidence [22, 60], where it shows the difference in plausibility from 1, so the sum of the belief, disbelief and uncertainty functions is equal to 1 [33].

No belief in the proposed target (i.e., $m\left(T_p\right)_{B_{ij}} = 0$) is when there has been no landslide in attribute $\mathrm{B_{ij}}$. In landslide studies, there will always be uncertainty, which does not mean disbelief in the complement $\mathrm{m}\,(\overline{\mathrm{T}}_{\mathrm{p}})_{\mathrm{B_{ij}}}$. Therefore, $\mathrm{m}\,(\overline{\mathrm{T}}_{\mathrm{p}})_{\mathrm{B_{ij}}}$ and consequently $\mathrm{m}\,(\theta)_{\mathrm{B_{ij}}}$ are 0 and 1, respectively. Landslide occurrence is related to the second complementary constraint. Therefore, in this case, landslides cannot occur at zero slope, and there is no belief in $\mathrm{m}\left(\mathrm{T_p}\right)_{\mathrm{B_{ij}}}$. On the basis of the first constraints, the disbelief and $\mathrm{m}\,(\theta)_{\mathrm{B_{ij}}}$ are set to 0 and 1, respectively; however, the disbelief must be 1 if the second constraints are met. Therefore, $\mathrm{m}\left(\mathrm{T_p}\right)_{\mathrm{B_{ij}}}$ and $\mathrm{m}\,(\theta)_{\mathrm{B_{ij}}}$ are set as 0, and $\mathrm{m}\,(\overline{\mathrm{T}}_{\mathrm{p}})_{\mathrm{B_{ij}}}$ is set as 1 in the relatively flat region [21].

Considering that the DS model is adopted from Bayesian theory, the natural logarithm of the probability ratio $\lambda(\mathrm{T_P})\mathrm{B_{ij}}$ and its opposite $(\lambda(\mathrm{T_P})\mathrm{B_{ij}})$ are equal to each positive and negative weight, which is considered equivalent to Eq.6 and Eq.7 of the final weight of the weight of evidence (WoE) model [21]. Therefore, both can be utilized to verify the weight as a conditioning factor of the binary map where the negative weight = 0 and positive weight = 1. Therefore, the landslide susceptibility map is calculated from the DS model and the weighting of the conditioning factor and the sum of the algebraic values of the belief function value (Eq.12).

$$\mathrm{LSI(DS)} = \sum_{\mathrm{j=1}}^{\mathrm{n}} (\mathrm{Bel})_{\mathrm{ij}} \qquad \text{(Eq.12)}$$

where $(\mathrm{Bel})_{\mathrm{ij}}$ is the belief value of class i in parameter j and where n represents the number of variables.

5.2) Statistical indices

The statistical index model was introduced by van Westen et al. [62] to identify potential landslide zones and has been widely adopted by researchers [18, 29]. This approach assesses each category weight unit as the natural logarithm of the landslide density in the category unit, which is then divided by the landslide density in the entire area [29]. This approach is formulated through Eq.13 [62]:

$$\mathrm{W_{ij}} = \ln\left(\frac{\mathrm{E_{ij}}}{\mathrm{E}}\right) = \ln\left(\frac{\frac{\mathrm{N_{ij}}}{\mathrm{S_{ij}}}}{\frac{\mathrm{N}}{\mathrm{S}}}\right) \qquad \text{(Eq.13)}$$

where $\mathrm{W_{ij}}$ is the weight of a particular class-I on parameter j; E_{ij} is the landslide density class-i on parameter j; E is the total landslide density in the entire area; $\mathrm{N_{ij}}$ is the number of landslides in a particular class-i of parameter j; $\mathrm{S_{ij}}$ is the number of pixels in a particular class-i on parameter j; and N and S are the total landslide and total pixels in the entire area, respectively. The higher the resultant weight is, the higher the probability of landslides in the class under consideration in the covered area.

5.3) Certainty factor

The certainty factor (CF) method is an approach used to reconcile differences and uncertainties identified in values (inputs). This method is also utilized to resolve any issues that may arise when all heterogeneous data layers are summed [19]. The formula used to calculate the CF value is shown in Eq.14.

$$\mathrm{CF} = \begin{cases} \frac{\mathrm{pp_a} - \mathrm{pp_s}}{\mathrm{pp_a}(1-\mathrm{pp_s})}, \text{if } \mathrm{pp_a} \geq \mathrm{pp_s} \\ \frac{\mathrm{pp_a} - \mathrm{pp_s}}{\mathrm{pp_s}(1-\mathrm{pp_a})}, \text{if } \mathrm{pp_a} < \mathrm{pp_s} \end{cases} \qquad \text{(Eq.14)}$$

where $\mathrm{pp_a}$ is the conditional probability of a landslide occurring in category a and where $\mathrm{pp_s}$ is the prior probability of the total number of landslides in the entire region.

The CF value ranges from -1 to 1, where a positive value indicates an increase in the certainty of a landslide, and vice versa. If the value approaches 0, it indicates a prior probability that tends to be similar to the conditional probability so that the certainty of a landslide becomes difficult to determine [24].

The CF values of the causal factors obtained are then combined into pairs on the basis of the CF combination rule. The pairwise CF value concatenation is formulated via Eq.15 [63–64].

$$\mathrm{Z} = \begin{cases} \mathrm{X} + \mathrm{Y} - \mathrm{XY} & \mathrm{X, Y} \geq 0 \\ \mathrm{X} + \mathrm{Y} + \mathrm{XY} & \mathrm{X, Y} < 0 \\ \frac{\mathrm{X+Y}}{1-\min(|\mathrm{X}|,|\mathrm{Y}|)} & \mathrm{X, Y\ opposite\ sign} \end{cases} \qquad \text{(Eq.15)}$$

The combination of two CF values, X and Y, from two different layers of information, where the Z value of the CF is obtained. Pairwise combination is carried out with Eq.15 until all the CF layers are combined and a landslide susceptibility map is produced.

Results and discussion

1) Landslide susceptibility via Dempster-Shafer

The landslide susceptibility model is calculated via the DS model. The actual landslide location is used to calculate the DS value. The results of the DS calculation are presented in Table 2, where each shows the mass functions $m\left(T_p\right)_{B_{ij}}$, $m\left(\overline{T}_p\right)_{B_{ij}}$, and $m(\Theta)$ calculated for each belief, disbelief, and plausibility function in Eqs.9 to 11. This model relies on the belief function to show the correlation between landslide conditioning factor categories and landslide events. The higher the belief function is, the stronger the relationship between the conditioning factor categories and landslide events and the greater the chance of landslides [33]. Indirectly, a higher belief function in a class results in a lower disbelief function and plausibility. The height factor shows that classes 100-400 and 400-700 have the highest belief and then disbelief with respect to other classes (Table 2). The slope class >45% shows the highest belief. The aspect category shows that the North and South classes have the same highest belief, which is 0.128 (Table 2). The curvature category shows that the convex class has the highest belief and the lowest disbelief. This condition is caused by high shear stress, minimal structural support and erosion factors in slope mechanics (Table 2). The TWI category shows that class <8 has the highest belief with the lowest disbelief (Table 2). Most studies have shown that a high TWI is more susceptible to landslides [65–66]. Pidies have many steep areas and thin soils, making them prone to sudden landslides during heavy rains. Historical data in Geumpang clearly show this pattern [67–68]. The SPI category shows that classes 3-7 have the highest belief compared with the other classes (Table 2). High-energy erosion followed by water thrusts, such as those in the Tangse, Geumpang, and Mane areas, which have many subwatersheds and tributaries, is very susceptible to landslides. Many studies have revealed similar findings, especially on slopes near the flow, not in the main river [69–70]. SPI class 61-185 has the highest belief and is most highlighted in Krueng Baro, Tiro, and Geumpang (Table 2). Although it does not directly trigger landslides, its effect is sufficient to trigger riverbank erosion and undercutting.

The land cover classes with high belief functions are dry fields, bushes, and mixed plantations (Table 3). The NDVI value of class 0.7-0.9 has the highest belief in this case, indicating the potential for it to occur (Table 4). Although this value is good for slope stability, the combination of extreme rain, extreme slopes and soil weathering, and earthquakes can still cause landslides to occur. This is in accordance with what the media reported [71]. The rainfall category of class 2250-2500 has a high level of belief, with the lowest level of disbelief (Table 4). This rainfall is quite significant as the main trigger, especially in areas with complex geological and topographic conditions.

For the distance to features (drainage, fault, and road), the belief function fluctuates, and then, the disbelief function decreases as the distance to these features increases (Tables 3 to 5). Microgabbro Rob (Mirb) is the lithology with the highest belief function, which is 0.25, whereas most other formations have a belief function = 0 (Table 5). The Microgabbro Rob is classified as susceptible to landslides, especially if it is located in areas with high rainfall, steep slopes, and intense weathering. Although dense, tropical weathering can cause weathering of clay soil (saprolite), which has low cohesion when saturated with water [72–73]. Geumpang, Tangse, and Mane (as highlighted in the susceptibility map) are real examples in the study area.

The final landslide susceptibility map was then created via the DS model (Table 2) with Eq.16.

The final LSM value range of the calculated DS model varies from 0.33-4.21. The values are then normalized to 0 to 1. The range of values is then reclassified into five classes (very low, low, moderate, high, and very high) via the natural breaks method (Figure 4a).

The observed landslide distribution is divided into vulnerability classes from different landslide vulnerability maps (Figure 6a). Approximately 10.22% fall into the very low category. The low-, moderate-, and high-vulnerability classes cover areas of 20.76%, 26.14%, and 27.40%, respectively. The very high vulnerability class accounts for 15.48% of the total area. Moreover, the total percentages of landslides in the very low-, low-, moderate-, high-, and very high-vulnerability classes are 0.21%, 2.30%, 15.67%, 32.08%, and 49.74%, respectively.

2) Landslide susceptibility via a statistical index

Landslide vulnerability is analyzed from the landslide conditioning factor to the landslide location with the SI model and is shown in Table 3. The elevation factor in classes 100-400 has the highest SI value (0.853), followed by classes 400-700 (0.616). However, it is clear that up to an altitude of 1,600-1,900, the probability of landslides decreases, whereas an altitude of 1,900-2,788 shows no relationship. For the slope factor, the class >45% had the highest SI correlation value. For the aspect factor, the North and South classes have the highest correlations, namely, 0.153 and 0.152, respectively. For curvature, the convex class (0.130) has the highest SI value, followed by the concave class (0.039). The flat class has a negative correlation with landslides. Class <8 in the TWI factor has a positive correlation (0.082), whereas the other classes have a negative relationship. This condition is also indicated by the SPI and STI factors, where only classes 3-7 and 61-185, respectively, have positive correlations (0.086 and 0.222), whereas the other classes have negative correlations. Moreover, classes 14-17 (SPI) and -1 to -0 (STI) have no relationship.

Table 2 The spatial relationships between landslides and topographic conditioning factors generated by the DS, SI, and CF models

Conditioning factors	Class	No. of pixel	No. of Landslide	Dempster-Shafer			Statistical index	Certainty factor		
				$\mathbf{m}\,(\mathbf{T_p})_{\mathbf{B_{ij}}}$	$\mathbf{m}\,(\overline{\mathbf{T}}_{\mathbf{p}})_{\mathbf{B_{ij}}}$	$\mathbf{m}(\boldsymbol{\Theta})$	$\mathbf{W_{ij}}$	$\mathbf{pp_a}$	$\mathbf{pp_s}$	**CF**
Elevation	0-100	737,338	150	0.039	0.119	0.841	-1.345	0.00020	0.00078	-0.74
	100-400	473,724	868	0.353	0.079	0.568	0.853	0.00183	0.00078	0.57
	400-700	531,209	768	0.279	0.085	0.636	0.616	0.00145	0.00078	0.46
	700-1,000	602,232	545	0.174	0.097	0.729	0.148	0.00090	0.00078	0.14
	1,000-1,300	554,448	407	0.142	0.101	0.757	-0.062	0.00073	0.00078	-0.06
	1,300-1,600	343,404	21	0.012	0.110	0.878	-2.547	0.00006	0.00078	-0.92
	1,600-1,900	177,980	1	0.001	0.105	0.894	-4.934	0.00001	0.00078	-0.99
	1,900-2,200	86,080	0	0.000	0.102	0.898	0.000	0.00000	0.00078	-1.00
	2,200-2,500	24,577	0	0.000	0.101	0.899	0.000	0.00000	0.00078	-1.00
	2,500-2,788	4,603	0	0.000	0.100	0.900	0.000	0.00000	0.00078	-1.00
Slope	0-8	1,065,960	496	0.111	0.235	0.654	-0.517	0.00047	0.00078	-0.40
	8-15	773,024	756	0.233	0.186	0.581	0.225	0.00098	0.00078	0.20
	15-25	953,002	952	0.238	0.179	0.583	0.247	0.00100	0.00078	0.22
	25-45	720,983	533	0.176	0.203	0.621	-0.054	0.00074	0.00078	-0.05
	>45	22,626	23	0.242	0.200	0.558	0.264	0.00102	0.00078	0.23
Aspect	Flat	41,673	2	0.007	0.101	0.892	-2.789	0.00005	0.00078	-0.94
	North	248,364	226	0.128	0.099	0.773	0.153	0.00091	0.00078	0.14
	North East	476,597	408	0.121	0.098	0.781	0.092	0.00086	0.00078	0.09
	East	430,029	361	0.118	0.099	0.783	0.073	0.00084	0.00078	0.07
	South East	423,646	381	0.127	0.098	0.775	0.142	0.00090	0.00078	0.13
	South	454,454	413	0.128	0.098	0.774	0.152	0.00091	0.00078	0.14
	South West	484,484	428	0.125	0.098	0.778	0.124	0.00088	0.00078	0.12
	West	385,596	209	0.076	0.104	0.820	-0.365	0.00054	0.00078	-0.31
	North West	381,013	177	0.066	0.105	0.830	-0.519	0.00046	0.00078	-0.40
	North	209,739	155	0.104	0.100	0.795	-0.055	0.00074	0.00078	-0.05
Curvature	Concave	874,963	710	0.336	0.329	0.335	0.039	0.00081	0.00078	0.04
	Flat	1,775,258	1,263	0.295	0.363	0.342	-0.093	0.00071	0.00078	-0.09
	Convex	885,374	787	0.369	0.318	0.314	0.130	0.00089	0.00078	0.12
TWI	<8	2,857,847	2421	0.214	0.453	0.333	0.082	0.00085	0.00078	0.08
	8-12	477,033	231	0.353	0.259	0.388	-0.478	0.00048	0.00078	-0.38
	>12	200,715	108	0.340	0.288	0.373	-0.372	0.00054	0.00078	-0.31
SPI	-1-3	933,194	578	0.246	0.215	0.539	-0.231	0.00062	0.00078	-0.21
	3-7	2,396,656	2,039	0.338	0.162	0.500	0.086	0.00085	0.00078	0.08
	7-11	188,724	138	0.290	0.201	0.509	-0.065	0.00073	0.00078	-0.06
	11-14	15,797	5	0.126	0.201	0.674	-0.903	0.00032	0.00078	-0.59
	14-17	1,224	0	0.000	0.200	0.800	0.000	0.00000	0.00078	-1.00
STI	-1-0	1	0	0.000	0.200	0.800	0.000	0.00000	0.00078	-1.00
	0-61	3,401,870	2,654	0.291	0.203	0.506	-0.001	0.00078	0.00078	-0.00
	61-185	82,084	80	0.363	0.199	0.438	0.222	0.00097	0.00078	0.20
	185-497	30,351	21	0.258	0.200	0.542	-0.121	0.00069	0.00078	-0.11
	>497	21,289	5	0.088	0.201	0.712	-1.201	0.00023	0.00078	-0.70

Table 3 The spatial relationships between landslides and anthropogenic conditioning factors generated by the DS, SI, and CF models

Conditioning factors	Class	No. of pixel	No. of Landslide	Dempster-Shafer			Statistical index	Certainty factor		
				$\mathbf{m}\,(\mathbf{T_p})_{\mathbf{B_{ij}}}$	$\mathbf{m}\,(\overline{\mathbf{T}}_{\mathbf{p}})_{\mathbf{B_{ij}}}$	$\mathbf{m}(\Theta)$	$\mathbf{W_{ij}}$	$\mathbf{pp_a}$	$\mathbf{pp_s}$	**CF**
Distance from road	0-100	130,857	10	0.019	0.172	0.809	-2.324	0.00008	0.00078	-0.90
	100-200	108,266	63	0.142	0.168	0.690	-0.294	0.00058	0.00078	-0.25
	200-300	91,343	88	0.234	0.166	0.600	0.210	0.00096	0.00078	0.23
	300-400	78,765	87	0.269	0.165	0.566	0.347	0.00110	0.00078	0.29
	400-500	69,608	40	0.140	0.168	0.693	-0.306	0.00057	0.00078	-0.26
	>500	3,056,756	2,472	0.197	0.128	0.675	0.035	0.00081	0.00078	0.04
LULC	Hp	1,816,534	155	0.007	0.139	0.855	-2.214	0.00009	0.00078	-0.89
	Hs	296,436	530	0.143	0.063	0.794	0.829	0.00179	0.00078	0.56
	B	491,179	1,348	0.219	0.042	0.739	1.257	0.00274	0.00078	0.71
	Pk	1,758	0	0.000	0.071	0.929	0.000	0.00000	0.00078	-1.00
	Pm	116,814	0	0.000	0.074	0.926	0.000	0.00000	0.00078	-1.00
	T	25,820	147	0.454	0.068	0.478	1.987	0.00569	0.00078	0.86
	S	81,612	13	0.013	0.073	0.915	-1.589	0.00016	0.00078	-0.80
	A	11,299	0	0.000	0.072	0.928	0.000	0.00000	0.00078	-1.00
	Pt	58,784	9	0.012	0.072	0.915	-1.629	0.00015	0.00078	-0.80
	Pc	291,845	558	0.153	0.062	0.785	0.896	0.00191	0.00078	0.59
	Sw	296,477	0	0.000	0.078	0.922	0.000	0.00000	0.00078	-1.00
	Tm	46,494	0	0.000	0.072	0.928	0.000	0.00000	0.00078	-1.00
	Tr	279	0	0.000	0.071	0.929	0.000	0.00000	0.00078	-1.00
	Pb	264	0	0.000	0.071	0.929	0.000	0.00000	0.00078	-1.00

Table 4 The spatial relationships between landslides and environmental conditioning factors generated by the DS, SI, and CF models

Conditioning factors	Class	No. of pixel	No. of Landslide	Dempster-Shafer			Statistical index	Certainty factor		
				$\mathbf{m}\,(\mathbf{T_p})_{\mathbf{B_{ij}}}$	$\mathbf{m}\,(\overline{\mathbf{T}}_{\mathbf{p}})_{\mathbf{B_{ij}}}$	$\mathbf{m}(\boldsymbol{\Theta})$	$\mathbf{W_{ij}}$	$\mathbf{pp_a}$	$\mathbf{pp_s}$	**CF**
NDVI	-2-0.1	19,804	0	0.000	0.201	0.799	0.000	0.00000	0.00078	-1.00
	0.1-0.3	46,458	2	0.023	0.203	0.775	-2.898	0.00004	0.00078	-0.94
	0.3-0.5	346,286	4	0.006	0.221	0.773	-4.213	0.00001	0.00078	-0.99
	0.5-0.7	1,756,623	1,037	0.310	0.248	0.441	-0.279	0.00059	0.00078	-0.24
	0.7-0.9	1,366,424	1,717	0.661	0.123	0.216	0.476	0.00126	0.00078	0.38
Rainfall	<2,000	679,909	0	0.000	0.177	0.823	0.000	0.00000	0.00078	-1.00
	2,000-2,250	204,200	118	0.099	0.145	0.756	-0.301	0.00058	0.00078	-0.26
	2,250-2,500	125,692	260	0.355	0.134	0.511	0.974	0.00207	0.00078	0.62
	2,500-2,750	509,289	185	0.062	0.156	0.782	-0.765	0.00036	0.00078	-0.53
	2,750-3,000	596,412	281	0.081	0.154	0.765	-0.505	0.00047	0.00078	-0.40
	3,000-3,250	1,007,356	1,601	0.272	0.084	0.644	0.711	0.00159	0.00078	0.51
	>3,250	412,737	315	0.131	0.143	0.726	-0.023	0.00076	0.00078	-0.02
Distance from river	0-200	1,208,255	911	0.190	0.204	0.607	-0.035	0.00075	0.00078	-0.03
	200-400	880,793	615	0.176	0.207	0.617	-0.112	0.00070	0.00078	-0.11
	400-600	562,622	597	0.267	0.186	0.547	0.307	0.00106	0.00078	0.26
	600-800	349,221	275	0.198	0.200	0.602	0.009	0.00079	0.00078	0.01
	>800	534,704	362	0.170	0.205	0.625	-0.142	0.00068	0.00078	-0.13

Table 5 The spatial relationships between landslides and geology conditioning factors generated by the DS, SI, and CF models

Conditioning factors	Class	No. of pixel	No. of Landslide	Dempster-Shafer			Statistical index	Certainty factor		
				$\mathbf{m}\,(\mathbf{T_p})_{\mathbf{B_{ij}}}$	$\mathbf{m}\,(\overline{\mathbf{T}}_{\mathbf{p}})_{\mathbf{B_{ij}}}$	$\mathbf{m}(\boldsymbol{\Theta})$	$\mathbf{W_{ij}}$	$\mathbf{pp_a}$	$\mathbf{pp_s}$	**CF**
Distance from fault	0-1,000	213,935	360	0.153	0.116	0.731	0.768	0.00168	0.00078	0.54
	1,000-2,000	203,378	517	0.232	0.108	0.660	1.181	0.00254	0.00078	0.69
	2,000-3,000	188,242	403	0.195	0.113	0.692	1.009	0.00214	0.00078	0.63
	3,000-4,000	181,731	194	0.097	0.123	0.780	0.313	0.00107	0.00078	0.27
	4,000-5,000	167,377	124	0.068	0.125	0.807	-0.052	0.00074	0.00078	-0.05
	5,000-6,000	162,321	227	0.128	0.120	0.752	0.583	0.00140	0.00078	0.44
	6,000-7,000	162,812	172	0.096	0.123	0.781	0.303	0.00106	0.00078	0.26
	>7,000	2,255,799	763	0.031	0.250	0.719	-0.836	0.00034	0.00078	-0.57

Table 5 The spatial relationships between landslides and geology conditioning factors generated by the DS, SI, and CF models *(continued)*

Conditioning factors	Class	No. of pixel	No. of Landslide	Dempster-Shafer			Statistical index	Certainty factor		
				$\mathbf{m}\ (\mathbf{T_p})_{\mathbf{B_{ij}}}$	$\mathbf{m}\ (\overline{\mathbf{T}}_{\mathbf{p}})_{\mathbf{B_{ij}}}$	$\mathbf{m}(\boldsymbol{\Theta})$	$\mathbf{W_{ij}}$	$\mathbf{pp_a}$	$\mathbf{pp_s}$	**CF**
Lithology	Qh	661,542	712	0.021	0.022	0.956	0.321	0.00108	0.00078	0.27
	Tb	6,777	0	0.000	0.024	0.976	0.000	0.00000	0.00078	-1.00
	Mumb	16,560	135	0.161	0.023	0.815	2.346	0.00815	0.00078	0.90
	Tbg	59,464	3	0.001	0.025	0.974	-2.739	0.00005	0.00078	-0.94
	Qtpsl	18,452	0	0.000	0.025	0.975	0.000	0.00000	0.00078	-1.00
	Mullr	23,917	0	0.000	0.025	0.975	0.000	0.00000	0.00078	-1.00
	Tuktm	44,099	197	0.088	0.023	0.889	1.744	0.00447	0.00078	0.82
	Bps	163,297	0	0.000	0.026	0.974	0.000	0.00000	0.00078	-1.00
	Tukts	42,660	89	0.041	0.024	0.935	0.983	0.00209	0.00078	0.63
	Tsn	20,859	0	0.000	0.025	0.975	0.000	0.00000	0.00078	-1.00
	Tlmj	24,375	11	0.009	0.024	0.967	-0.548	0.00045	0.00078	-0.42
	Misk	71,409	13	0.004	0.025	0.972	-1.456	0.00018	0.00078	-0.77
	Miski	4,161	0	0.000	0.024	0.976	0.000	0.00000	0.00078	-1.00
	Qvo	7,412	0	0.000	0.024	0.976	0.000	0.00000	0.00078	-1.00
	Tps-me	9	0	0.000	0.024	0.976	0.000	0.00000	0.00078	-1.00
	Tps-sa	116,112	0	0.000	0.025	0.975	0.000	0.00000	0.00078	-1.00
	Ttb	138,434	0	0.000	0.025	0.975	0.000	0.00000	0.00078	-1.00
	Tla	60,707	323	0.105	0.022	0.873	1.919	0.00532	0.00078	0.85
	Tmg	6,737	0	0.000	0.024	0.976	0.000	0.00000	0.00078	-1.00
	Tbs	2,328	0	0.000	0.024	0.976	0.000	0.00000	0.00078	-1.00
	Mutlr	12,661	0	0.000	0.024	0.976	0.000	0.00000	0.00078	-1.00
	Mugl	278,755	27	0.002	0.026	0.972	-2.087	0.00010	0.00078	-0.88
	Tgm	11,730	0	0.000	0.024	0.976	0.000	0.00000	0.00078	-1.00
	Tjl	137,134	4	0.001	0.025	0.974	-3.287	0.00003	0.00078	-0.96
	Tukt	132,143	225	0.034	0.023	0.943	0.780	0.00170	0.00078	0.54
	Tk	289,530	3	0.000	0.027	0.973	-4.322	0.00001	0.00078	-0.99
	Mum	48,914	318	0.129	0.022	0.849	2.120	0.00650	0.00078	0.88
	Tlm	413,809	149	0.007	0.026	0.967	-0.774	0.00036	0.00078	-0.54
	Qtps	84,856	0	0.000	0.025	0.975	0.000	0.00000	0.00078	-1.00
	Tsm	97,321	0	0.000	0.025	0.975	0.000	0.00000	0.00078	-1.00
	Tsp	119,016	0	0.000	0.025	0.975	0.000	0.00000	0.00078	-1.00
	Tib	6,197	0	0.000	0.024	0.976	0.000	0.00000	0.00078	-1.00
	Tbi	9,200	0	0.000	0.024	0.976	0.000	0.00000	0.00078	-1.00
	Ppm	65,765	0	0.000	0.025	0.975	0.000	0.00000	0.00078	-1.00
	Tmigs	132,099	284	0.043	0.023	0.935	1.013	0.00215	0.00078	0.64
	Mirb	2,452	31	0.250	0.024	0.725	2.785	0.01264	0.00078	0.94
	TI	109,724	0	0.000	0.025	0.975	0.000	0.00000	0.00078	-1.00
	Qm	13,234	0	0.000	0.024	0.976	0.000	0.00000	0.00078	-1.00
	Mpn	25,809	0	0.000	0.025	0.975	0.000	0.00000	0.00078	-1.00
	Tuset	45,351	236	0.103	0.023	0.874	1.897	0.00520	0.00078	0.85
	Kus	10,584	0	0.000	0.024	0.976	0.000	0.00000	0.00078	-1.00

$$\begin{aligned}\mathrm{LSI_{DS}} = (&\left(\mathrm{Elevation} \times \mathrm{m}\,(\theta)_{\mathrm{B_{ij}}}\right) + (\left(\mathrm{Slope} \times \mathrm{m}\,(\theta)_{\mathrm{B_{ij}}}\right) + (\left(\mathrm{Aspect} \times \mathrm{m}\,(\theta)_{\mathrm{B_{ij}}}\right) \\ &+ (\left(\mathrm{Curvature} \times \mathrm{m}\,(\theta)_{\mathrm{B_{ij}}}\right) + (\left(\mathrm{TWI} \times \mathrm{m}\,(\theta)_{\mathrm{B_{ij}}}\right) + (\left(\mathrm{SPI} \times \mathrm{m}\,(\theta)_{\mathrm{B_{ij}}}\right) \\ &+ (\left(\mathrm{STI} \times \mathrm{m}\,(\theta)_{\mathrm{B_{ij}}}\right) + (\left(\mathrm{NDVI} \times \mathrm{m}\,(\theta)_{\mathrm{B_{ij}}}\right) + (\left(\mathrm{Rainfall} \times \mathrm{m}\,(\theta)_{\mathrm{B_{ij}}}\right) \\ &+ (\left(\mathrm{Distance\ from\ River} \times \mathrm{m}\,(\theta)_{\mathrm{B_{ij}}}\right) + (\left(\mathrm{Distance\ from\ Road} \times \mathrm{m}\,(\theta)_{\mathrm{B_{ij}}}\right) \\ &+ (\left(\mathrm{Distance\ from\ Fault} \times \mathrm{m}\,(\theta)_{\mathrm{B_{ij}}}\right) + (\left(\mathrm{LULC} \times \mathrm{m}\,(\theta)_{\mathrm{B_{ij}}}\right) + ((\mathrm{Lithology} \\ &\times \mathrm{m}\,(\theta)_{\mathrm{B_{ij}}})\end{aligned} \quad \text{(Eq.16)}$$

where $\mathrm{LSI_{DS}}$ represents the landslide susceptibility calculated via the DS model.

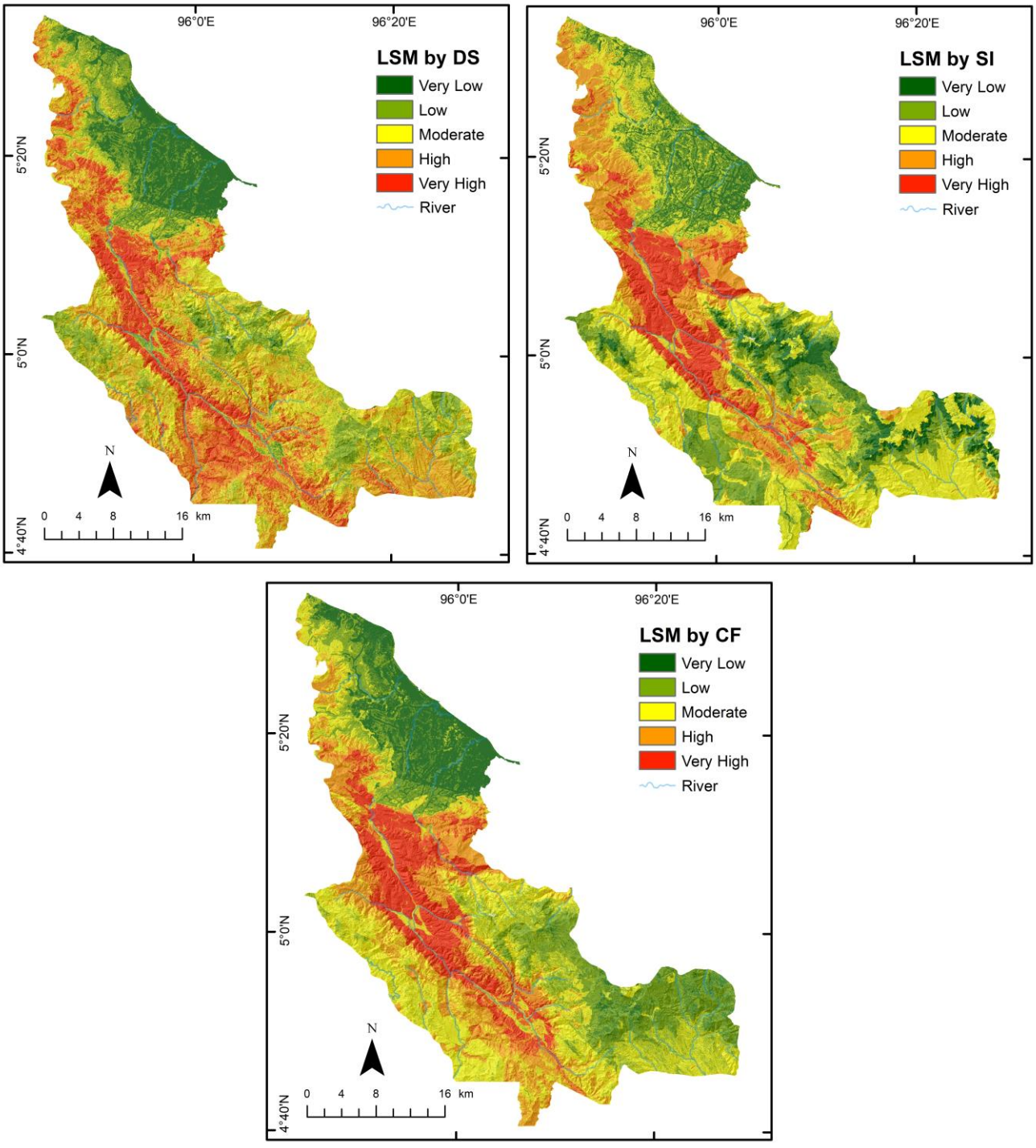

Figure 4 The landslide susceptibility model is derived from a) DS model, b) SI model, and c) CF model.

For the distance from the road factor, the highest positive SI value is shown by classes 300-400. Unlike other distance features, the distance from the fault factor has a negative correlation only in classes 4000-5000 and >7000, whereas other classes have positive SI values, with the highest SI being in classes 2000-3000. For the LULC factor, the class with the highest positive SI value was dry fields, followed by shrubs and mixed plantations, with values of 1.987, 1.257, and 0.896, respectively.

For the NDVI factor, classes 0.7-0.9 had a positive correlation (0.476), whereas the other classes had a negative correlation (class 0.1-0.7) and no relationship (-2 to 1). For the rainfall factor, only classes 2250-2500 and 3000-3250 had positive SI values of 0.974 and 0.711, respectively, and the other classes had negative correlations. The distance from the river factor shows that classes 400-600 and 600-800 have positive SI values of 0.307 and 0.009, respectively. For the lithology factor, Mirb has the highest positive value, with an SI value of 2.785.

The landslide susceptibility map via the SI method is then produced from the calculation results in Table 3 via Eq.17.

Therefore, with Eq.17, the final landslide susceptibility map via the SI method was generated with a range of values between -14.99 and 8.06 and reclassified into five classes, namely, very low, low, moderate, high, and very high (Figure 4b). Among the five susceptibility zones (Figure 6b), the very low susceptibility zone covers 12.51%, and the low, moderate, high, and very high susceptibility zones cover 22.90%, 32.81%, 19.33%, and 12.45%, respectively. In addition, approximately 81.40% and 13.38% of the total landslides fall in the very high and high susceptibility zones, respectively. The moderate, low, and very low susceptibility zones cover approximately 3.45%, 1.46%, and 0.31%, respectively.

3) Landslide susceptibility via certainty factors

The landslide susceptibility from this model uses the CF values from Table 3 calculated via Eq.14. For the elevation factor, the highest CF value is shown by classes 100-400 (0.57), followed by classes 400-700 (0.46) and classes 700-1000 (0.14). For the slope factor, the highest CF is shown by the slope class >45%. Similar to DS and SI, the aspect class with the highest CF value is North China, and South China has the same value. For the curvature factor, the convex class has the highest CF value (0.12), followed by the concave class (0.04). The TWI shows that only class <8 has a positive relationship with landslide occurrence. Similarly, the SPI (3-7 = 0.08), STI (61-185 = 0.20), and NDVI (0.7-0.9 = 0.38) were used. For the rainfall conditioning factor, positive CF values are indicated by classes 2250-2500 (0.62) and classes 3000-3250 (0.51).

The distance factor from the feature shows a different pattern. In terms of the distance from the river, the highest CF value is indicated by class 400-600 (0.26), followed by class 600-800 (0.01). The distance from the road factor shows that class 300-400 has the highest CF, namely, 0.29, followed by 200-300 = 0.23 and >500 = 0.04. The distance from the fault factor indicates that the closer the distance of the landslide event is to the fault, the greater the increase in the CF value. The highest CF value is indicated by class 1000-2000 (0.69), and the lowest is in class 6000-7000 (0.26). For the LULC factor, the highest positive CF value is shown by the dry land class (0.86), followed by shrubs (0.71), mixed plantations (0.59), and secondary dry land forests (0.56). Like the SI model, for the lithology factor, Mirb also has the highest positive value, with a CF value of 0.94.

The landslide susceptibility map via the CF method is generated from the calculations in Table 3 via Eq.18.

On the basis of Eq.18, the final landslide vulnerability map via the CF method is also produced, with values ranging between -1 and 0.97. The model output is then reclassified into five classes, namely, very low, low, moderate, high, and very high (Figure 4c). The distribution of different landslide zone vulnerability classes was observed in this study (Figure 6c). The largest vulnerability zone was the moderate class, namely, 29.35%, followed by the low class (23.28%), high class (20.01%), very high class (13.84%), and very low class (13.51%) of the total area. The total distribution of landslides from the largest to the smallest is shown by the very high class (79.00%), high (16.72%), moderate (3.76%), low (0.31%), and very low (0.21%) total number of landslide events observed.

$$\begin{aligned} \mathrm{LSI_{SI}} = {} & \mathrm{W_{SI}\,(Elevation)} + \mathrm{W_{SI}\,(Slope)} + \mathrm{W_{SI}\,(Aspect)} + \mathrm{W_{SI}\,(Curvature)} + \mathrm{W_{SI}\,(TWI)} \\ & + \mathrm{W_{SI}\,(SPI)} + \mathrm{W_{SI}\,(STI)} + \mathrm{W_{SI}\,(NDVI)} + \mathrm{W_{SI}\,(Rainfall)} \\ & + \mathrm{W_{SI}\,(Distance\ from\ River)} + \mathrm{W_{SI}\,(Distance\ from\ Road)} \\ & + \mathrm{W_{SI}\,(Distance\ from\ Fault)} + \mathrm{W_{SI}\,(LULC)} + \mathrm{W_{SI}\,(Lithology)} \end{aligned} \quad \text{(Eq.17)}$$

where $\mathrm{LSI_{SI}}$ represents the landslide susceptibility calculated via the SI model.

$$\begin{aligned} LSI_{CF} = {} & W_{CF}\,(\text{Elevation}) + W_{CF}\,(\text{Slope}) + W_{CF}\,(\text{Aspect}) + W_{CF}\,(\text{Curvature}) + W_{CF}\,(\text{TWI}) \\ & + W_{CF}\,(\text{SPI}) + W_{CF}\,(\text{STI}) + W_{CF}\,(\text{NDVI}) + W_{CF}\,(\text{Rainfall}) \\ & + W_{CF}\,(\text{Distance from River}) + W_{CF}\,(\text{Distance from Road}) \\ & + W_{CF}\,(\text{Distance from Fault}) + W_{CF}\,(\text{LULC}) + W_{CF}\,(\text{Lithology}) \end{aligned} \quad \text{(Eq.18)}$$

where LSI_{CF} is the landslide susceptibility calculated via the cf model.

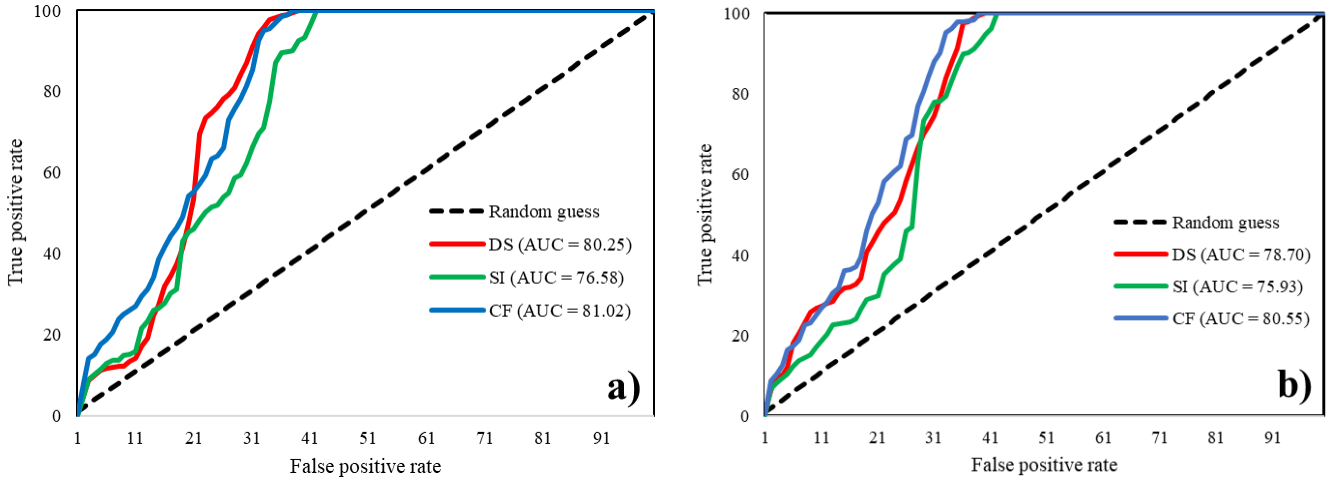

Figure 5 The AUC representing the quality of the models: a) success rate curve and b) prediction rate curve.

4) Validation of the landslide susceptibility maps

Spatial model validation is important for determining the reliability of the evaluation results in a structured manner [74]. The area under the curve (AUC) method is used to check this. This method works by creating a specific rate curve to explain the percentage of known landslides at each previously determined vulnerability level, where the results are presented as a cumulative frequency diagram [75]. The specific rate curve is divided into a success rate curve and a prediction rate curve [76]. The success rate curve describes the level of suitability on the basis of the comparison of vulnerability with landslides [76–77]. The prediction rate curve indicates the ability of the model to predict the vulnerability of a map. The rate curves show the cumulative percentage of the vulnerability class area on the x-axis and the percentage of cumulative landslide occurrences in different vulnerability classes on the y-axis. Both can be used to qualitatively determine the accuracy of the vulnerability model. Generally, the larger the area is, the higher the accuracy [75].

The success-rate curve and prediction-rate curve are presented in Figure 5. The AUCs for the success-rate curve in the DS, SI, and CF models are 80.25%, 76.58%, and 81.02%, respectively. The AUCs for the overall prediction rate curve are 78.70%, 75.93%, and 80.55%, respectively. These results indicate that the three models do not differ much in terms of performance. The three models are also considered successful estimators and are able to predict landslide-prone locations well, considering that the accuracy produced is quite good in the study area. The AUC curve revealed that CF increased faster in the early stages than did the other two models did (Figure 5). This finding indicates that the sensitivity of the CF model is relatively high in predicting landslide susceptibility.

Zhao et al. [78] calculated the success rate and prediction rate of CF at 70.48% and 68.86%, respectively. Moreover, the SI model had a success rate and prediction rate of 70.19% and 68.67%, respectively. These results indicate a lower probability than that observed. However, the distribution and frequency of landslides grouped in training and testing datasets should not be ignored [76]. However, comparisons of CF and DS are still very limited. The study by Binaghi et al. [64] is one of the few references that reviews the comparison of both. The strength of the DS model seems to be due to the synergy of integrity with other methods rather than the theoretical ability of the DS model as a single model. In contrast, the CF model shows competitive performance even as a standalone model. This finding indicates that CF is more reliable in the context of independent modeling for landslide susceptibility zoning. Other studies also report better CF capabilities than other models, such as IV, SI, WoE, LR, AHP, and WoA [30,78–82]. Research can provide a scientific basis for governments and policy makers and support spatial planning and disaster mitigation in vulnerable areas.

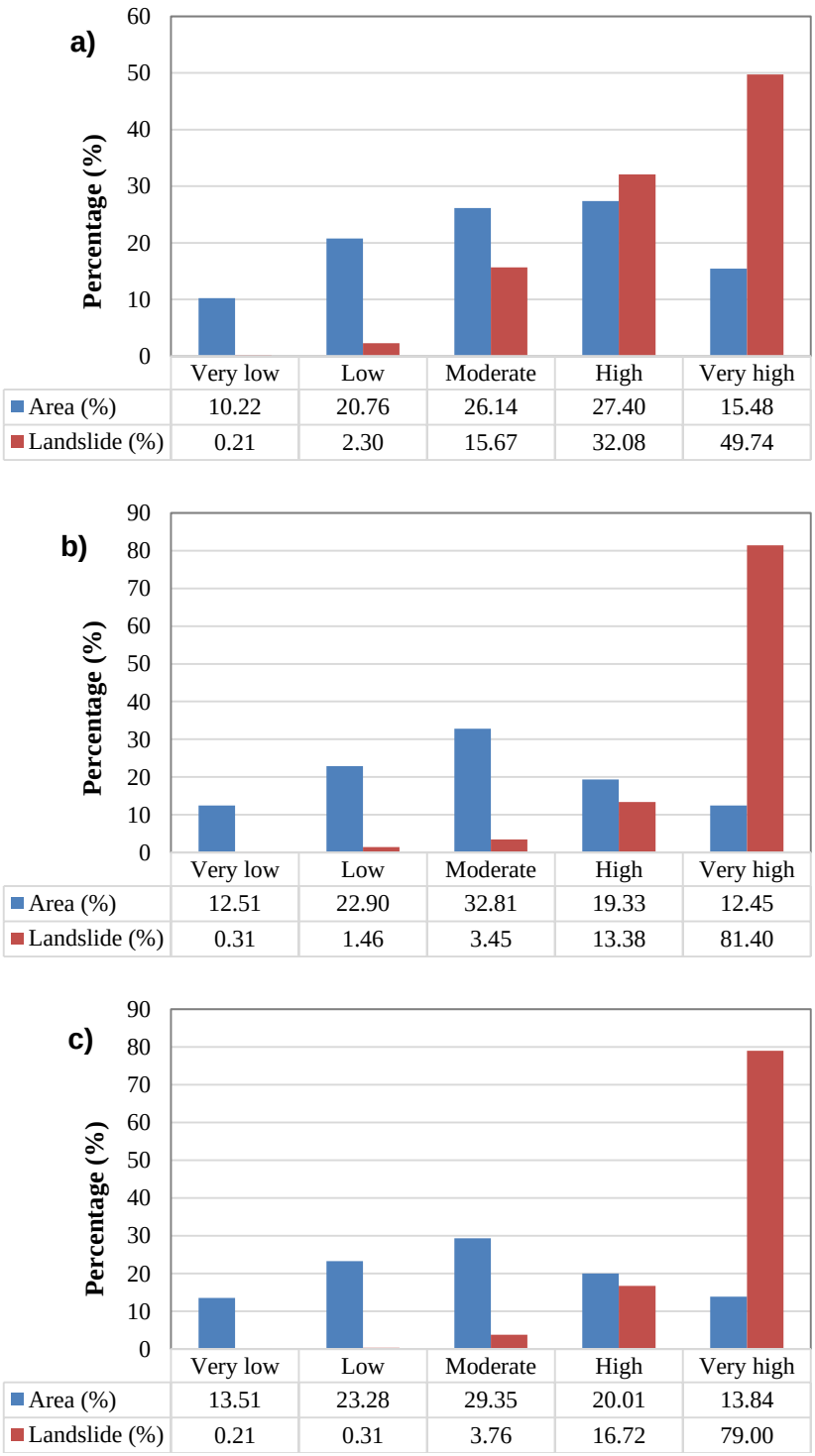

Figure 6 Distribution of observed landslides into susceptibility classes of landslide susceptibility zonation maps: a) DS model, b) SI model, and c) CF model.

5) Sustainable development goals relevant to landslides

The 17 Sustainable Development Goals (SDGs) are linked to the most pressing global challenges. They encompass various social, economic, and environmental dimensions, with progress in all areas dependent on progress in these areas. These goals emphasize a more integrated approach, partnerships, and collective action in addressing complex global issues, leaving no one behind and ensuring that the benefits of development reach even the most vulnerable segments of society [83–85]. While no SDG is explicitly dedicated to landslides, several goals implicitly address this issue. One such goal is Goal 1: No poverty. Poverty reduction plays a crucial role in enhancing community resilience to natural hazards such as landslides. Addressing poverty indirectly improves access to resources, infrastructure, and services. This is considered to contribute to more sustainable land-use planning, housing development, and the implementation of early warning systems in areas most prone to landslides. Goal 11: Sustainable cities and communities are equally relevant. This goal

emphasizes the importance of inclusive, safe, resilient, and sustainable cities. Improvements in urban planning, infrastructure development, and disaster mitigation measures in the most vulnerable areas are considered to reduce community vulnerability to landslides. This indirectly ensures public safety and well-being.

The SDGs also address climate issues in Goal 13: climate action, which addresses landslide risk reduction. Climate change significantly impacts landslide occurrence through shifts in rainfall patterns, increases in extreme weather events, and other factors. Addressing climate change can reduce landslide vulnerability and impacts by implementing appropriate mitigation and adaptation measures. Furthermore, Goal 15 addresses the promotion of sustainable land management practices by conserving landscapes and forests. These efforts can reduce landslide risk by maintaining slope stability, reducing erosion, and protecting biodiversity. By focusing on more sustainable land-use practices and long-term ecosystem conservation, communities can help improve landslide resilience and terrestrial ecosystem health.

The SDGs provide a broad framework, but landslides are not explicitly mentioned. However, this goal indirectly includes landslide risk mitigation by addressing sustainable development practices, climate action, and disaster mitigation strategies. All of these goals highlight the interconnectedness of the environment, poverty reduction, spatial and regional planning, and climate change mitigation and adaptation. Given the crucial impact of landslides, governments, organizations, and communities need to be encouraged to achieve inclusive and sustainable development. While there may be updates or developments related to landslides beyond the current state of knowledge, the SDGs provide a strong foundation for upholding actions deemed to reduce landslide risk and increase overall community resilience in the face of natural disasters.

Conclusions

This study used Dempster-shafer, a statistical index, and a certainty factor for landslide susceptibility assessment in Pidie Regency, Aceh, Indonesia. The three methods were built from elevation, slope, aspect, curvature, TWI, SPI, STI, NDVI, rainfall, distance from feature (river, road, and fault), LULC, and lithology factors. The use of these 14 factors was based on considerations of the relevance, availability, and scale of the data that were considered appropriate for the regional scale, which were relative and subjective. Therefore, the selection of conditioning factors in the study could be improved. This study identified and mapped approximately 957 total landslide events. On the basis of this number, 670 locations (70%) were randomly used to build the model, and the remaining 287 locations (30%) were used for model validation. The susceptibility map in this study was divided into five classes, namely, very low, low, moderate, high, and very high. The accuracy test reveals that the success rates of the DS, SI, and CE models are 80.25%, 76.58%, and 81.02%, respectively, whereas the prediction rates are 78.70%, 75.93%, and 80.55%, respectively. It is clear that the three models do not perform much differently. The results of this study highlight that the determination of appropriate conditioning factors together with the DS, SI, and CF methods, as well as the application of geographic information systems, are considered capable of describing areas prone to landslides. However, the resulting model is built from basic assumptions such as topography, hydrology, vegetation, and anthropogenic factors. In addition to other factors, such as geomorphology, nonhydrometeorology (peak ground acceleration), and temporal influences (seasons and changes in time), the resulting analysis can be more accurate.

While landslides are not explicitly addressed within the SDGs, several goals—namely, Goal 1 (No Poverty), Goal 11 (Sustainable Cities and Communities), Goal 13 (Climate Action), and Goal 15 (Life on Land)—implicitly contribute to landslide risk reduction. Efforts toward poverty reduction, resilient urban development, climate change adaptation, and sustainable land management provide indirect yet significant pathways to enhance slope stability and community resilience. Accordingly, the SDGs offer a comprehensive framework through which disaster risk reduction, including landslide mitigation, can be systematically integrated into broader sustainable development agendas.

The results of this study can help decision makers, managers, engineers, and land use developers with actual slope management and evaluation and spatial and regional planning. This research methodology can also be used to analyze landslide vulnerability in other regions in Indonesia or in other regions that are considered to have similar geological and topographic features. Future research should integrate higher-resolution datasets, incorporate geomorphological and seismic factors, and apply advanced integrated machine learning techniques to improve the model's robustness and predictive accuracy. Furthermore, temporal analyses that consider seasonal variations and long-term land-use changes are needed to produce more dynamic and realistic landslide susceptibility assessments.

References

[1] L Lee, M.J., Choi, J.W., Oh, H.J., Won, J.S., Park, I., Lee, S. Ensemble-based landslide susceptibility maps in Jinbu area, Korea. Environmental Earth Sciences, 2012, 67, 23–37.

[2] Chen, W., Pourghasemi, H.R., Kornejady, A., Zhang, N. Landslide spatial modeling: Introducing new ensembles of ANN, MaxEnt, and SVM machine learning techniques. Geoderma 2017, 305, 314–327.

[3] Shirani, K. Modelling of landslide susceptibility zonation using Shannon's entropy index and weight of evidence model (Case Study: Sarkhoon's Karoon). Journal of Water and Soil Science 2017, 21, 51–68.

[4] BNPB. Risiko Bencana Indonesia-Memahami Risiko Sistemik di Indonesia. 1st edition. Jakarta: Pusat Data Informasi Komunikasi Bencana BNPB; 2023.

[5] JICA. Signing of Japanese ODA loan agreement with Indonesia: Support construction and rehabilitation facilities related to fishing ports and markets contributing to development of fishery sector, and support rehabilitation and construction the sediment control. 2024.

[6] Tien Bui, D., Tuan, T.A., Klempe, H., Pradhan, B., Revhaug, I. Spatial prediction models for shallow landslide hazards: A comparative assessment of the efficacy of support vector machines, artificial neural networks, kernel logistic regression, and logistic model tree. Landslides 2016, 13, 361–378.

[7] Dai, F.C., Lee, C.F. Landslide characteristics and slope instability modeling using GIS, Lantau Island, Hong Kong. Geomorphology 2002, 42, 213–228.

[8] Pourghasemi, H.R., Rossi, M. Landslide susceptibility modeling in a landslide prone area in Mazandarn Province, north of Iran: A comparison between GLM, GAM, MARS, and M-AHP methods. Theoretical and Applied Climatology, 2017, 130, 609–633.

[9] Guzzetti, F., Reichenbach, P., Cardinali, M., Galli, M., Ardizzone, F. Probabilistic landslide hazard assessment at the basin scale. Geomorphology 2005, 72, 272–299.

[10] Guzzetti, F., Mondini, A.C, Cardinali, M., Fiorucci, F., Santangelo, M., Chang, K.T. Landslide inventory maps: New tools for an old problem. Earth-Science Reviews, 2012, 112, 42–66.

[11] Varnes, D.J. Landslide hazard zonation: A review of principles and practice. Paris: UNESCO, 1984.

[12] Gokceoglu, C., Sezer, E. A statistical assessment on international landslide literature (1945–2008). Landslides, 2009, 6, 345–351.

[13] van Westen, C.J., van Asch, T.W.J., Soeters, R. Landslide hazard and risk zonation—why is it still so difficult? Bulletin of Engineering Geology and the Environment, 2006, 65, 167–184.

[14] Yilmaz, I. Landslide susceptibility mapping using frequency ratio, logistic regression, artificial neural networks and their comparison: A case study from Kat landslides (Tokat—Turkey). Computers & Geosciences, 2009, 35, 1125–1138.

[15] Yalcin, A. GIS-based landslide susceptibility mapping using analytical hierarchy process and bivariate statistics in Ardesen (Turkey): Comparisons of results and confirmations. Catena (Amst) 2008, 72, 1–12.

[16] Akgun, A., Dag, S., Bulut, F. Landslide susceptibility mapping for a landslide-prone area (Findikli, NE of Turkey) by likelihood-frequency ratio and weighted linear combination models. Environmental Geology, 2008, 54, 1127–1143.

[17] Lee, S., Talib, J.A. Probabilistic landslide susceptibility and factor effect analysis. Environmental Geology, 2005, 47, 982–990.

[18] Yesilnacar, E., Topal, T. Landslide susceptibility mapping: A comparison of logistic regression and neural networks methods in a medium scale study, Hendek region (Turkey). Engineering Geology, 2005, 79, 251–666.

[19] Devkota, K.C., Regmi, A.D., Pourghasemi, H.R., Yoshida, K., Pradhan, B., Ryu, I.C, ... Althuwaynee, O.F. Landslide susceptibility mapping using certainty factor, index of entropy and logistic regression models in GIS and their comparison at Mugling–Narayanghat road section in Nepal Himalaya. Natural Hazards, 2013, 65, 135–65.

[20] Chen, W., Li, W., Hou, E., Bai, H., Chai, H., Wang, D., ... Wang, Q. Application of frequency ratio, statistical index, and index of entropy models and their comparison in landslide susceptibility mapping for the Baozhong Region of Baoji, China. Arabian Journal of Geosciences, 2015, 8, 1829–1841.

[21] Park, N.W. Application of Dempster-Shafer theory of evidence to GIS-based landslide susceptibility analysis. Environmental Earth Sciences, 2011, 62, 367–376.

[22] Althuwaynee, O.F., Pradhan, B., Lee, S. Application of an evidential belief function model in landslide susceptibility mapping. Computers & Geosciences, 2012, 44, 120–135.

[23] Mohammady, M., Pourghasemi, H.R., Pradhan, B. Landslide susceptibility mapping at Golestan Province, Iran: A comparison between frequency ratio, Dempster–Shafer, and weights-of-evidence models. Journal of Asian Earth Sciences, 2012, 61, 221–236.

[24] Pourghasemi, H., Pradhan, B., Gokceoglu, C., Moezzi, K.D. A comparative assessment of prediction capabilities of Dempster–Shafer and Weights-of-evidence models in landslide susceptibility mapping using GIS. Geomatics, Natural Hazards and Risk, 2013, 4, 93–118.

[25] Chen, W., Pourghasemi, H.R., Naghibi, S.A. A comparative study of landslide susceptibility maps produced using support vector machine with different kernel functions and entropy data mining models in China. Bulletin of Engineering Geology and the Environment, 2018, 77, 647–664.

[26] Ding, Q., Chen, W., Hong, H. Application of frequency ratio, weights of evidence and evidential belief function models in landslide susceptibility mapping. Geocarto International, 2016, 1–21.

[27] Youssef, A.M., Pradhan, B., Pourghasemi, H.R., Abdullahi, S. Landslide susceptibility assessment at Wadi Jawrah Basin, Jizan region, Saudi Arabia using two bivariate models in GIS. Geosciences Journal, 2015, 19, 449–469.

[28] Chen, W., Pourghasemi, H.R., Zhao, Z. A GIS-based comparative study of Dempster-Shafer, logistic regression and artificial neural network models for landslide susceptibility mapping. Geocarto International, 2017, 32, 367–385.

[29] Regmi, A.D., Devkota, K.C., Yoshida, K., Pradhan, B., Pourghasemi, H.R., Kumamoto, T., Akgun, A. Application of frequency ratio, statistical index, and weights-of-evidence models and their comparison in landslide susceptibility mapping in Central Nepal Himalaya. Arabian Journal of Geosciences, 2014, 7, 725–742.

[30] Chen, W., Li, W., Chai, H., Hou, E., Li, X., Ding, X. GIS-based landslide susceptibility mapping using analytical hierarchy process (AHP) and certainty factor (CF) models for the Baozhong region of Baoji City, China. Environmental Earth Sciences, 2016, 75, 63.

[31] Chen, W., Panahi, M., Pourghasemi, H.R. Performance evaluation of GIS-based new ensemble data mining techniques of adaptive neuro-fuzzy inference system (ANFIS) with genetic algorithm (GA), differential evolution (DE), and particle swarm optimization (PSO) for landslide spatial modelling. Catena (Amst), 2017, 157, 310–324.

[32] Wang, Q., Li, W., Chen, W., Bai, H. GIS-based assessment of landslide susceptibility using certainty factor and index of entropy models for the Qianyang County of Baoji city, China. Journal of Earth System Science, 2015, 124, 1399–1415.

[33] Wang, Q., Li, W., Wu, Y., Pei, Y., Xing, M., Yang, D. A comparative study on the landslide susceptibility mapping using evidential belief function and weights of evidence models. Journal of Earth System Science, 2016, 125, 645–662.

[34] Chen, W., Pourghasemi, H.R, Zhao, Z. A GIS-based comparative study of Dempster-Shafer, logistic regression and artificial neural network models for landslide susceptibility mapping. Geocarto International, 2017, 32, 367–385.

[35] Pradhan, B. Landslide susceptibility mapping of a catchment area using frequency ratio, fuzzy logic and multivariate logistic regression approaches. Journal of the Indian Society of Remote Sensing, 2010, 38, 301–320.

[36] Pradhan, B. An Assessment of the use of an advanced neural network model with five different training strategies for the preparation of landslide susceptibility maps. Journal of Data Science, 2011, 9, 65–81.

[37] Lee, S., Choi, J. Landslide susceptibility mapping using GIS and the weight-of-evidence model. International Journal of Geographical Information Science, 2004, 18, 789–814.

[38] Roodhiyah, L.Y., Nurhasan., Tiffany., Pratomo, P.M., Susilawati, A., Supriyadi., ... Srigutomo, W. Interpretation of a 3D Magnetotellurics model of the Aceh and Seulimeum segments of the Sumatran fault zone. Applied Sciences, 2024, 14, 11335.

[39] Waiyasusri, K., Chotpantarat, S. Spatial evolution of coastal tourist city using the Dyna-CLUE model in Koh Chang of Thailand during 1990–2050. ISPRS International Journal of Geo-Information, 2022, 11, 49.

[40] Kiriwongwattana, K., Waiyasusri, K. Spatial evolution of smart cities for sustainable tourism: A case study of Phuket Province, Thailand. GeoJournal of Tourism and Geosites, 2024, 55, 1312–1320.

[41] Waiyasusri, K., Tananonchai, A. Spatio-temporal development of coastal tourist city over the last 50 years from Landsat Satellite Image perspective in Takua Pa District, Phang-Nga Province, Thailand. GeoJournal of Tourism and Geosites, 2022, 43, 937–945.

[42] BMKG. Peta Rata-Rata Curah Hujan dan Hari Hujan Periode 1991-2020 Indonesia. Jakarta: Pusat Informasi Perubahan Iklim BMKG, 2021.

[43] Sivakami, C., Rajkumar, D.R. Landslide vulnerability zone by weights of evidence model using remote sensing and GIS, in Kodaikanal Taluk (Tamil nadu, India). International Journal of Engineering Research & Technology, 2020, 9, 788-793.

[44] Aldiansyah, S., Wardani, F. Assessment of resampling methods on performance of landslide susceptibility predictions using machine learning in Kendari City, Indonesia. Water Practice & Technology, 2024, 19, 52–81.

[45] Hong, H., Chen, W., Xu, C., Youssef, A.M, Pradhan, B., Tien Bui, D. Rainfall-induced landslide susceptibility assessment at the Chongren area (China) using frequency ratio, certainty factor, and index of entropy. Geocarto International, 2016, 1–16.

[46] Bui, D.T., Pradhan, B., Revhaug, I., Nguyen, D.B., Pham, H.V., Bui, Q.N. A novel hybrid evidential belief function-based fuzzy logic model in spatial prediction of rainfall-induced shallow landslides in the Lang Son city area (Vietnam). Geomatics, Natural Hazards and Risk, 2015, 6, 243–271.

[47] Hong, H., Pourghasemi, H.R., Pourtaghi, Z.S. Landslide susceptibility assessment in Lianhua County (China): A comparison between a random forest data mining technique and bivariate and

multivariate statistical models. Geomorphology, 2016, 259, 105–118.

[48] Akgun, A., Sezer, E.A., Nefeslioglu, H.A., Gokceoglu, C., Pradhan, B. An easy-to-use MATLAB program (MamLand) for the assessment of landslide susceptibility using a Mamdani fuzzy algorithm. Computers & Geosciences, 2012, 38, 23–34.

[49] Dou, J., Tien Bui, D, P. Yunus, A., Jia, K., Song, X., Revhaug, I., ... Zhu, Z. Optimization of causative factors for landslide susceptibility evaluation using remote sensing and GIS data in parts of Niigata, Japan. PLoS One, 2015, 10, e0133262.

[50] Kornejady, A., Ownegh, M., Rahmati, O., Bahremand, A. Landslide susceptibility assessment using three bivariate models considering the new topo-hydrological factor: HAND. Geocarto International 2018, 33, 1155–1185.

[51] Pachauri, A.K., Pant, M. Landslide hazard mapping based on geological attributes. Engineering Geology, 1992, 32, 81–100.

[52] Anbalagan, R. Landslide hazard evaluation and zonation mapping in mountainous terrain. Engineering Geology, 1992, 32, 269–277.

[53] Lee, S., Min, K. Statistical analysis of landslide susceptibility at Yongin, Korea. Environmental Geology, 2001, 40, 1095–1113.

[54] Guillard, C., Zezere, J. Landslide susceptibility assessment and validation in the framework of municipal planning in Portugal: The case of Loures Municipality. Environmental Management, 2012, 50, 721–735.

[55] Ramesh, V., Anbazhagan, S. Landslide susceptibility mapping along Kolli hills Ghat road section (India) using frequency ratio, relative effect and fuzzy logic models. Environmental Earth Sciences, 2015, 73, 8009–8021.

[56] Sonker, I., Tripathi, J.N, Singh, A.K. Landslide susceptibility zonation using geospatial technique and analytical hierarchy process in Sikkim Himalaya. Quaternary Science Advances, 2021, 4, 100039.

[57] Moore, I.D., Grayson, R.B., Ladson, A.R. Digital terrain modelling: A review of hydrological, geomorphological, and biological applications. Hydrological Process, 1991, 5, 3–30.

[58] Pourghasemi, H.R., Mohammady, M., Pradhan, B. Landslide susceptibility mapping using index of entropy and conditional probability models in GIS: Safarood Basin, Iran. Catena (Amst), 2012, 97, 71–84.

[59] Shahabi, H., Ahmad, B.B., Khezri, S. Application of Satellite remote sensing for detailed landslide inventories using frequency ratio model and GIS. International Journal of Computer Science Issues, 2012, 9, 108–117.

[60] Tien Bui, D., Pradhan, B., Lofman, O., Revhaug, I., Dick, O.B. Spatial prediction of landslide hazards in Hoa Binh province (Vietnam): A comparative assessment of the efficacy of evidential belief functions and fuzzy logic models. Catena (Amst), 2012, 96, 28–40.

[61] Liu, Y., Cheng, Q., Xia, Q., Wang, X. The use of evidential belief functions for mineral potential mapping in the Nanling belt, South China. Frontier of Earth Science, 2015, 9, 342–354.

[62] Van Westen, C.J. Statistical landslide hazard analysis ILWIS 2.1 for Windows application guide. Enschede: ITC Publication, 1997.

[63] Chung, C.J.F., Fabbri, A.G. The representation of geoscience information for data integration. Nonrenewable Resources, 1993, 2, 122–139.

[64] Binaghi, E., Luzi, L., Madella, P., Pergalani, F., Rampini, A. Slope instability zonation: A comparison Between Certainty Factor and Fuzzy Dempster–Shafer Approaches. Natural Hazards, 1998, 17, 77–97.

[65] Mengstie, L., Nebere, A., Jothimani, M., Taye, B. Landslide susceptibility assessment in Addi Arkay, Ethiopia using GIS, remote sensing, and AHP. Quaternary Science Advances, 2024, 15, 100217.

[66] Alam, S.A., Mandal, S., Maiti, R. Geospatial intelligence for landslide susceptibility and risk analysis: Insights from NH31A and east Sikkim Himalaya settlements. Natural Hazards Research, 2025, 5, 187–208.

[67] Pusat Krisis Kesehatan. Tanah Longsor di PIDIE, ACEH, 2017. [Online] Available from: https://pusatkrisis.kemkes.go.id/tanah-longsor-di-pidie-aceh--11-07-2017? (Accessed 26 May 2025).

[68] Pusat Krisis Kesehatan. Tanah-Longsor di PIDIE, ACEH-, 2021. [Online] Available from: https://pusatkrisis.kemkes.go.id/Tanah-Longsor-di-PIDIE-ACEH--10-07-2021-40? (Accessed 26 May 2025).

[69] Sun, X., Chen, J., Bao, Y., Han, X., Zhan, J., Peng, W. Landslide susceptibility mapping using logistic regression analysis along the Jinsha river and its tributaries close to Derong and Deqin County, Southwestern China. ISPRS International Journal of Geo-Information, 2018, 7, 438.

[70] Yi, X., Shang, Y., Liang, S., Meng, H., Meng, Q., Shao P., Cui, Z. Landslide susceptibility mapping considering landslide spatial aggregation using the dual-frequency ratio method: A case study on the middle reaches of the Tarim River Basin. Remote Sens (Basel), 2025, 17, 381.

[71] ESDM. 4 Warga Mane, Pidie yang Meninggal Tertimbun Longsor Mencari Emas di Kawasan Hutan Lindung, 2021. [online] Available from: https://esdm.acehprov.go.id/berita/kategori/esdm-aceh/4-warga-mane-pidie-yang-meninggal-tertimbun-longsor-mencari-emas-di-kawasan-hutan-lindung? (Accessed 19 May 2025).

[72] Lee, J.U, Cho, Y.C., Kim, M., Jang, S.J., Lee, J., Kim, S. The effects of different geological conditions on landslide-triggering rainfall conditions in South Korea. Water (Basel) 2022, 14, 2051.

[73] Li, L., Li, G.K., Li, L., Li, G. Landslide-induced weathering in tectonically active mountains: evidence from dissolved radiogenic uranium isotopes. Frontier in Earth Science (Lausanne), 2022, 10.

[74] Ahmed, B., Ahmed, R., Zhu, X. Evaluation of model validation techniques in land cover dynamics. ISPRS International Journal of Geo-Information, 2013, 2, 577–597.

[75] Intarawichian, N., Dasananda, S. Frequency ratio model based landslide susceptibility mapping in lower Mae Chaem watershed, Northern Thailand. Environmental Earth Sciences, 2011, 64, 2271–2285.

[76] Chung, C.J.F., Fabbri, A.G. Validation of spatial prediction models for landslide hazard mapping. Natural Hazards, 2003, 30, 451–472.

[77] Pradhan, A.M.S., Kim, Y.T. Relative effect method of landslide susceptibility zonation in weathered granite soil: A case study in Deokjeok-ri Creek, South Korea. Natural Hazards, 2014, 72, 1189–1217.

[78] Zhao, C., Chen, W., Wang, Q., Wu, Y., Yang, B. A comparative study of statistical index and certainty factor models in landslide susceptibility mapping: A case study for the Shangzhou District, Shaanxi Province, China. Arabian Journal of Geosciences, 2015, 8, 9079–9088.

[79] Wang, Q., Guo, Y., Li, W., He, J., Wu, Z. Predictive modeling of landslide hazards in Wen County, northwestern China based on information value, weights-of-evidence, and certainty factor. Geomatics, Natural Hazards and Risk, 2019, 10, 820–835.

[80] Mandal, S., Mondal, S. Weighted overlay analysis (WOA) model, certainty factor (CF) model and analytical hierarchy process (AHP) model in landslide susceptibility studies. Cham: Springer International Publishing, 2019, 135–162.

[81] Nahayo, L., Kalisa, E., Maniragaba, A., Nshimiyimana, F.X. Comparison of analytical hierarchy process and certain factor models in landslide susceptibility mapping in Rwanda. Modeling Earth System & Environment, 2019, 5, 885–895.

[82] Saha, A., Tripathi, L., Villuri, V.G.K., Bhardwaj. A. Exploring machine learning and statistical approach techniques for landslide susceptibility mapping in Siwalik Himalayan Region using geospatial technology. Environmental Science and Pollution Research, 2024, 31, 10443–10459.

[83] Hák, T., Janoušková, S., Moldan, B. Sustainable development goals: A need for relevant indicators. Ecological Indicators, 2016, 60, 565–573.

[84] Nanehkaran, Y. A., Chen, B., Cemiloglu, A., Chen, J., Anwar, S., Azarafza, M., Derakhshani, R. Riverside landslide susceptibility overview: Leveraging artificial neural networks and machine learning in accordance with the United Nations (UN) sustainable development goals. Water, 2023, 15, 2707.

[85] Yang, C., Wang, J., Li, S., Xiong, R., Li, X., Gao, L., Guo, X., Ma, C., Xiong, H., Qiu, Y. Landslide susceptibility assessment and future prediction with land use change and urbanization towards sustainable development: The case of the Li River valley in Yongding, China. Sustainability, 2024, 16, 4416.